Multinucleon pion absorption on ⁴He into the *pppn* final state

A. Lehmann,[1,8] D. Androić,[9] G. Backenstoss,[1] D. Bosnar,[9] H. Breuer,[4] H. Döbbeling,[8] T. Dooling,[7] M. Furić,[9]
P. A. M. Gram,[3] N. K. Gregory,[5] A. Hoffart,[2,8] C. H. Q. Ingram,[8] A. Klein,[7] K. Koch,[8] J. Köhler,[1] B. Kotliński,[8] M. Kroedel,[1]
G. Kyle,[6] A. O. Mateos,[5] K. Michaelian,[8] T. Petković,[9] M. Planinić,[9] R. P. Redwine,[5] D. Rowntree,[5] U. Sennhauser,[8]
N. Šimičević,[5] R. Trezeciak,[2] H. Ullrich,[2] M. Wang,[6] M. H. Wang,[6] H. J. Weyer,[1,8] M. Wildi,[1] and K. E. Wilson[5]

(LADS Collaboration)
[1]*University of Basel, CH-4056 Basel, Switzerland*
[2]*University of Karlsruhe, D-76128 Karlsruhe, Germany*
[3]*LAMPF, Los Alamos, New Mexico 87545*
[4]*University of Maryland, College Park, Maryland 20742*
[5]*Massachusetts Institute of Technology, Cambridge, Massachusetts 02139*
[6]*New Mexico State University, Las Cruces, New Mexico 88003*
[7]*Old Dominion University, Norfolk, Virginia 23529*
[8]*Paul Scherrer Institute, CH-5232 Villigen PSI, Switzerland*
[9]*University of Zagreb, HR-10000 Zagreb, Croatia*
(Received 18 June 1997)

Results from a 4π solid angle measurement of the reaction $\pi^{+}{}^{4}\text{He}\rightarrow pppn$ at incident pion energies of $T_{\pi^+}=$ 70, 118, 162, 239, and 330 MeV are presented. Integrated cross sections are given for the reactions where three nucleons participate, leading to energetic (ppp) or (ppn) final states, and for states where four nucleons are involved ($pppn$). The two three-nucleon absorption modes were investigated in particular, and an energy dependent isospin ratio of the cross sections of $\sigma_{ppn}/\sigma_{ppp}=3.6\pm1.3, 2.6\pm0.5, 1.8\pm0.3, 1.4\pm0.2$, and 1.8 ± 0.6 was determined from 70 to 330 MeV. The differential cross sections were described by a complete set of eight independent variables and compared to simple cascade and phase space models. From this analysis the contributions from initial state interactions to the multinucleon absorption cross sections were found to be more important at higher pion energies, while those from final state interactions are stronger at lower energies. However, both mechanisms combined were found to account for not more than one-third of the total $pppn$ multinucleon yield. The remaining strength is reasonably well reproduced by phase space models, but shows a dependence on the incident pion's orbital angular momentum. The isospin structure of the (ppp) and (ppn) final states is not understood, nor are some structures in their distributions. The four-nucleon yield ($pppn$) was found to be weak (1–8 % of the total absorption cross section) and shows no evidence for a ''double-Δ'' excitation. [S0556-2813(97)03210-X]

PACS number(s): 25.80.Ls, 25.10.+s, 21.45.+v, 13.75.Gx

I. INTRODUCTION

How a pion is absorbed by nuclei has been studied for almost 50 years [1–3]. It was found that the basic process involves two nucleons with, across the Δ-resonance region, the absorption on an isoscalar $T=0$ pair (2NA) being stronger by more than an order of magnitude than the absorption on an isovector $T=1$ pair. The ratio is a consequence of the Pauli principle that forbids some partial waves of the isovector mode to be in a ΔN intermediate state.

Although the pion absorption process on two nucleons is broadly understood theoretically [4], there remains the open question of where the experimentally measured yield of more than two nonspectator nucleons arises. Such a process was explicitly observed about 10 years ago in a kinematically complete experiment on ³He [5]. Since then several measurements have confirmed this result [6–12], but were unable to give a conventional explanation for the effect [13]. Only recently could part of this multinucleon yield clearly be attributed to a pion-nucleon rescattering preceding the absorption process [initial state interaction, (ISI)] [14–16]. Another ''conventional'' mechanism would be 2NA followed by a nucleon-nucleon interaction [final state interaction, (FSI)], which in He was not seen [13] or found to be small [16]. This weakness of the FSI was confirmed by a recent Faddeev-type calculation on ³He [17].

All investigations up to now have concluded that multinucleon pion absorption cannot easily be understood in terms of simple cascade processes only. A large fraction of the three-nucleon absorption (3NA) yield is distributed in phase space without clear kinematic signatures. Therefore, it was considered that 3NA might originate from an unknown mechanism which involves the three nucleons in a coherent way. An important key in this context could be the comparison of the two isospin different channels $^{4}\text{He}(\pi^{+},ppp)n$ and $^{4}\text{He}(\pi^{+},ppn)p$ (in this paper we use the nomenclature that the final state nucleons inside the brackets participated in the reaction while those outside were spectators, independent of whether they were detected). Because of different isospin couplings the cross section ratios and, of course, the distributions should give additional information about the importance of ISI and FSI in multinucleon pion absorption. For example, the ISI mechanism is expected to be weaker in the $^{4}\text{He}(\pi^{+},ppn)p$ channel, while the FSI

should be stronger. A previous work [18] on ^{4}He reported a ratio of $\sigma_{ppn}/\sigma_{ppp} \approx 2$ which is hard to understand in terms of the ISI being the main contributor to 3NA, while, on the other hand, no clear signatures of the FSI have been found up to now.

The only work that appears to explain this ratio approximately correctly assumes a one-step pion absorption process on a three-nucleon system [19]. This result was deduced from the isospin structure only without specifying the reaction mechanism, and shows that comparison of different isospin states may well shed more light on the puzzle of multinucleon pion absorption.

Another interesting question is the appearance of mechanisms where even more than three nucleons (4NA) were actively involved in the absorption process. Such processes were long ago proposed in the ''alpha-pole model'' [20] and later with the ''double-Δ'' mechanism [21,22]. Certainly, the yield of 4NA should also give more constraints on the importance of an ISI and FSI in pion absorption, since in a semiclassical cascade picture 4NA must originate from at least three-step processes.

Up to now there exists only one measurement where the total $pppn$ multinucleon pion absorption cross section on ^{4}He is decomposed into 3NA(ppp), 3NA(ppn), and 4NA ($pppn$) components [18]. The main reason for this is that at least three particles have to be completely measured in coincidence to fully describe the final state, and this was very difficult with the former low solid angle experiments.

Specifically for the 4NA cross section on ^{4}He there are four previous measurements [18,23–25]. At low incident pion energies the 4NA yield was found to be small [18,25], while its fraction appeared to become more important at higher energies [23–25].

This paper presents investigations of the multinucleon pion absorption on ^{4}He into the four-particle final state $pppn$. Five incident positive pion energies (70, 118, 162, 239, and 330 MeV) were measured with a 4π solid angle detector. The differential and integral cross sections of the two different 3NA isospin modes ^{4}He(π^+,ppp)n (see also Ref. [16]) and ^{4}He(π^+,ppn)p will be compared to each other in view of the ISI and FSI [both hard FSI (HFSI) and soft FSI (SFSI)]. The 4NA mode ^{4}He(π^+,$pppn$) will also be discussed.

II. EXPERIMENT

The data were taken with the Large Acceptance Detector System (LADS) [26]. This detector was built at the Paul Scherrer Institute (PSI) in Villigen, Switzerland, for a detailed investigation of multinucleon pion absorption modes. The large solid angle coverage ($\approx 98\%$ of 4π) and the low particle threshold ($T_{thr} \approx 20$ MeV for protons) together represent a significant improvement compared to previous pion absorption experiments.

The two main components of LADS were a modular scintillator array of 280 channels for energy spectroscopy and two coaxial, cylindrical multiwire proportional chambers (MWPC's) for determination of the charged particle trajectories. The scintillator array consisted of a plastic cylinder around the beam axis divided into 28 $\Delta E - E - E$ sectors, 1.6 m in active length and read out at both ends, and two 14

sector $\Delta E - E$ ''end-cap'' blocks to close the cylinder. The inner radius of the cylinder of 30 cm was enough to provide reasonable neutron-gamma discrimination by time of flight. The thickness of the E layers was designed to stop protons of up to 250 MeV and to detect about every third neutron. A specially developed high pressure (up to 100 bar) gas cylinder of 25.7 cm length and 2 cm radius with only 0.5 mm thick carbon-fiber/epoxy walls was used as a target.

The π^+ beam was defined by a set of thin plastic scintillation detectors that served to count the incident number of pions and to reject the beam halo. To suppress accidental coincidences with other beam bursts the master gate was closed for 60 ns before and after an event was registered. About 5% of the typically incident flux of more than 10^6 momentum-analyzed pions per s was finally accepted (N_{beam}) by a 2 cm diameter plastic counter upstream of the target.

III. INDEPENDENT KINEMATIC VARIABLES

The full breakup of ^{4}He after pion absorption leads to a four-particle final state. For the complete description of such a reaction eight independent variables are needed. Since we want to compare channels with three active particles (3NA) in particular, we will keep the independent variable set β, γ, ξ, ψ_{min}, and ψ_{max}, introduced in Ref. [16] to describe three particles, and extend it by three variables for the fourth particle. First, the three most energetic particles in the laboratory system (lab) are determined. The five variables listed above are calculated in the center of mass (c.m.) of these three particles, which are also labeled 1,2,3 in order of decreasing energy in this system. ξ and β are Euler angles describing, respectively, the angle between the normal to the three-particle plane and the incident beam and the azimuthal angle of that plane, while γ reflects the distribution of the protons within the plane; ψ_{min} and ψ_{max} are the minimum and maximum opening angles between pairs of the three particles. The three additional variables introduced here to describe the lowest lab energy particle (labeled 4) are also calculated in the three-particle c.m. system. These are the magnitude of the momentum of the fourth particle (p_{p4}), the angle between the fourth particle and the normal to the three-particle plane (ξ_{p4}), and the angle between the projections of the incident beam and the fourth particle on this plane (γ_{p4}). The formal definitions of these two angles are

$$\xi_{p4} = \arccos(\hat{\mathbf{n}} \cdot \hat{\mathbf{p}}_{p4}), \qquad (3.1)$$

$$\gamma_{p4} = \arccos\left(\frac{\hat{\mathbf{n}} \times (\hat{\mathbf{p}}_{p4} \times \hat{\mathbf{n}})}{|\hat{\mathbf{n}} \times (\hat{\mathbf{p}}_{p4} \times \hat{\mathbf{n}})|} \cdot \frac{\hat{\mathbf{n}} \times (\hat{\mathbf{p}}_{\pi} \times \hat{\mathbf{n}})}{|\hat{\mathbf{n}} \times (\hat{\mathbf{p}}_{\pi} \times \hat{\mathbf{n}})|} \right) \qquad (3.2)$$

with $\hat{\mathbf{n}} = (\hat{\mathbf{p}}_2 \times \hat{\mathbf{p}}_1)/|\hat{\mathbf{p}}_2 \times \hat{\mathbf{p}}_1|$ being the unit normal to the three-particle plane, $\hat{\mathbf{p}}_\pi$ the unit vector of the incident pion momentum in lab, $\hat{\mathbf{p}}_1$ and $\hat{\mathbf{p}}_2$ the unit vectors of the two highest energetic outgoing particle momenta in the three-body c.m. system, and $\hat{\mathbf{p}}_{p4}$ the unit vector of the fourth-particle momentum in the three-body c.m. system.

TABLE I. Summary of event generators used to simulate the different absorption mechanisms of the reaction $\pi^+ {}^4\text{He} \rightarrow pppn$. More detailed descriptions of the abbreviations are given in the text. Each σ represents a differential cross section as a function of the polar scattering angle. The ρ_N represents a one-nucleon momentum density distribution, and F_{pp} and F_{pn} the Jost enhancement functions.

Event generator	Weighting factors
$4\text{NA}_{(pppn)}$	$4\text{NA}_{(pppn)} * F_{pp} * F_{pn}$
$3\text{NA}_{(ppp)n}^{L \geqslant 0}$	$4\text{NA}_{(pppn)} * \rho_N * P_0[\cos(\xi)] * F_{pp} * F_{pn}$
$3\text{NA}_{(ppp)n}^{L \geqslant 1}$	$4\text{NA}_{(pppn)} * \rho_N * \{1 - P_2[\cos(\xi)]\} * F_{pp} * F_{pn}$
$\text{ISI}_{(ppp)n}$	$\rho_N * \rho_N * \sigma_{\pi^+ p \rightarrow \pi^+ p} * \sigma_{2\text{NA}} * F_{pp} * F_{pn}$
$\text{HFSI}_{(ppp)n}$	$\rho_N * \rho_N * \sigma_{2\text{NA}} * \sigma_{pp} * F_{pp} * F_{pn}$
$3\text{NA}_{(ppn)p}^{L \geqslant 0}$	$4\text{NA}_{(pppn)} * \rho_N * P_0[\cos(\xi)] * F_{pp} * F_{pn}$
$3\text{NA}_{(ppn)p}^{L \geqslant 1}$	$4\text{NA}_{(pppn)} * \rho_N * \{1 - P_2[\cos(\xi)]\} * F_{pp} * F_{pn}$
$\text{ISI}_{(ppn)p}^{\text{SCX}}$	$\rho_N * \rho_N * \sigma_{\pi^+ n \rightarrow \pi^0 p} * \sigma_{2\text{NA}} * F_{pp} * F_{pn}$
$\text{ISI}_{(ppn)p}$	$\rho_N * \rho_N * \sigma_{\pi^+ n \rightarrow \pi^+ n} * \sigma_{2\text{NA}} * F_{pp} * F_{pn}$
$\text{HFSI}_{(ppn)p}$	$\rho_N * \rho_N * \sigma_{2\text{NA}} * \sigma_{pn} * F_{pp} * F_{pn}$
$2\text{NA}_{(pp)pn}$	$4\text{NA}_{(pppn)} * \rho_N * \rho_N * \sigma_{2\text{NA}} * F_{pp} * F_{pn}$

IV. DATA ANALYSIS

A. Data treatment

The conditions for the reconstructed vertex were the same as in Ref. [16]: track information for all charged particles, and a vertex within 100 mm upstream and downstream of the target center and within 17 mm around the beam axis.

The proton identification, using kinetic energy, energy loss, and time-of-flight (TOF) information, was also done with the same cuts as those described in Ref. [16]. A neutron was assumed to be detected when a neutral hit in the E scintillators (no ΔE counter fired) deposited more than 8 MeV of light and had a reduced TOF (normalized to 30 cm flight path) of more than 1.5 ns. Neutral hits with shorter TOF were attributed to photons and were used to suppress single-charge-exchange (SCX) events.

For the events with three protons detected the measured four-momenta of the three protons were enough to reconstruct the neutron's four-momentum vector with good resolution. In these cases the reconstructed neutron momentum was always used in the analysis independent of whether the neutron was detected. This procedure does not work as well for those events, where only two protons and a neutron were detected. The short flight path and the thick scintillators do not permit good energy resolution for the neutron. Therefore the neutron angles, given by the time difference of the upstream and downstream pulse signals in the cylinder scintillators and by the segmentation of LADS ($\Delta\phi \approx \Delta\Theta \approx 13°$), were used together with the momenta of the two protons to reconstruct the neutron's kinetic energy and the momentum vector of the missing third proton. The missing mass resolution of about 25 MeV for these events was worse than that for events with three protons detected (10–13 MeV), but was enough to clean up the leftover SCX events with a cut of ± 120 MeV around the reconstructed proton mass. For consistency reasons, in the analysis presented in this paper the same wide cut was applied to the reconstructed neutron mass of the three-proton events. Corrections for events with reactions in the scintillator material were taken into account with the Monte Carlo simulations.

Also in this analysis events near the edge of the detector acceptance were eliminated by limiting the polar angular range to $15° - 165°$. Background events from misidentified deuterons were removed by rejecting events in which the neutron angle was within $8°$ of one of the protons, as discussed in Ref. [16].

B. Monte Carlo simulations

For the interpretation of the data Monte Carlo simulations were made. By tracking all simulated protons and neutrons through a model of the detector using the CERN GEANT software package, these could also be used to correct for acceptance and efficiency losses of the experimental data. The resolutions and hardware thresholds of the individual counters were folded into the simulations, the data from which were then run through the same analysis chain as the experimental data. After this procedure the effects of geometrical acceptance, reaction losses in the scintillators, and inefficiencies of the MWPC's and the reconstruction code were reflected in both the experimental and simulated distributions. Tests showed that this procedure is reliable [14,27–29].

Following the approach of Refs. [14,16] simple semiclassical models were used to represent various reaction mechanisms to assist the physics interpretation of the data. Eleven different event generators were found to be necessary for a full decomposition of the $pppn$ final state of ^{4}He (see Table I): one for the reaction ^{4}He$(\pi^+, pppn)$, four for ^{4}He $(\pi^+, ppp)n$, five for ^{4}He$(\pi^+, ppn)p$, and one for ^{4}He $(\pi^+, pp)pn$. The isovector 2NA reaction ^{4}He$(\pi^+, pn)pp$ is known to be weak [30] and was neglected in this analysis. The event generators used for the various reactions were the following.

($pppn$): Three protons and one neutron ($4N$) were generated with constant density in phase space ($4\text{NA}_{(pppn)}$).

(ppp)n: To model the one-step 3NA the neutron in the 4 N phase space distribution was weighted with a momentum distribution (ρ_N) from a calculation by Schiavilla [31,32] adjusted to fit ^{4}He$(e, e'p)^3$H data [33]. To take into account

angular momentum effects [16,34] the events of this generator were additionally weighted by the Legendre polynomials $P_0[\cos(\xi)]$ ($3NA^{L \geq 0}_{(ppp)n}$) and $\{1 - P_2[\cos(\xi)]\}$ ($3NA^{L \geq 1}_{(ppp)n}$). The distributions of (ISI+2NA) and (2NA+HFSI) were generated by an incoherent superposition of two elastic scattering processes. In the ISI model (ISI$_{(ppp)n}$) the pion was first scattered by one proton, moving with Fermi momentum (ρ_N), according to the differential elastic πp cross section ($\sigma_{\pi^+ p \to \pi^+ p}$, calculated with SCATPI [35]), before being absorbed on a quasideuteron recoiling from the pn system with a momentum distribution of ($\rho_N * \rho_N$), with the quasifree 2NA cross section (σ_{2NA}) [37]. A suppression of the forward pion quasielastic cross section was taken into account [16]. In the HFSI model (HFSI$_{(ppp)n}$) the pion was first absorbed on a quasideuteron moving with Fermi momentum opposite to that of the recoiling pn system ($\rho_N * \rho_N$), and then one of the outgoing protons was scattered off the recoil proton according to its differential elastic NN cross section (σ_{pp}), calculated with SAID [36] and with a minimum momentum transfer of 150 MeV/c. All these models were the same as in Ref. [16].

$(ppn)p$: The one-step 3NA models of this channel ($3NA^{L \geq 0}_{(ppn)p}$; $3NA^{L \geq 1}_{(ppn)p}$) were the same as for $(ppp)n$, except that instead of the neutron one of the protons was treated as a spectator with Fermi momentum distribution ρ_N. In this case there are two simple ISI modes that can feed the $(ppn)p$ channel: a quasielastic scattering of the π^+ on a neutron ($\sigma_{\pi^+ n \to \pi^+ n}$) and a charge-exchange reaction of the type $\pi^+ n \to \pi^0 p$ ($\sigma_{\pi^+ n \to \pi^0 p}$), both followed by the actual quasifree absorption (σ_{2NA}) on a quasideuteron. Both the mode with an initial elastic scattering (ISI$_{(ppn)p}$) and that with an initial SCX scattering (ISI$^{SCX}_{(ppn)p}$) were simulated as for ISI in the $(ppp)n$ channel. The proton and the neutron after the absorption of the π^0 emerging from the initial SCX process were simulated with the same angular distributions as $\pi^+ d \to pp$ (σ_{2NA}). The HFSI model (HFSI$_{(ppn)p}$) was also the same as for the $(ppp)n$ channel, except that in the second step one of the protons was scattered elastically off the neutron (σ_{pn}).

$(pp)pn$: In the quasifree 2NA model ($2NA_{(pp)pn}$) the neutron and one proton of the $4N$ phase space were each weighted according to their single-particle momentum distributions ρ_N. The absorption cross section was taken to be the same as that on a free deuteron (σ_{2NA}).

Each final state nucleon pair of all the event generators described was additionally weighted with the Jost enhancement functions F_{pp} and F_{pn} [38–40] to take into account the soft final state interaction (SFSI) of the Watson-Migdal type [41]. This effect changes some characteristics of the distributions of the $(ppn)p$ and $(pppn)$ channels quite significantly. The parameters used for proton-neutron SFSI were $r_0 = 2.60$ fm for the effective range and $a = -23.7$ fm for the scattering length [42]. For proton-proton SFSI $r_0 = 2.66$ fm and $a = -7.70$ fm were used.

C. Neutron detection efficiency

For a proper correction of the measured $(ppn)p$ cross sections for detection inefficiencies it has to be ensured that the neutron efficiencies are treated correctly in the simulations. Neutron reactions in the LADS Monte Carlo package
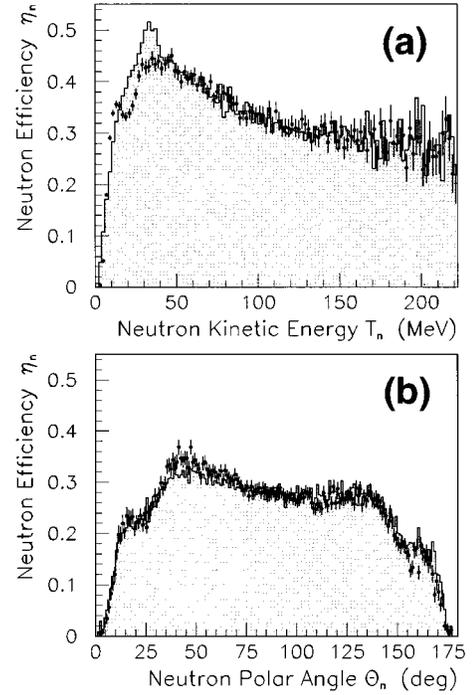

FIG. 1. Neutron detection efficiency η_n of LADS (dots with error bars) compared to Monte Carlo simulations (shaded area) as a function of the neutron kinetic energy (a) and the polar angle (b).

were handled by GEANT. For neutrons under 20 MeV the MICAP subroutine was used to calculate the reaction probabilities, while above this energy the FLUKA section of the code was applied.

To compare the neutron detection efficiencies in the experimental data and in the simulations, absorption events from ^{4}He with three detected protons were used and the neutron's angles and kinetic energy were reconstructed. The ratio of actually measured neutrons to those expected gave the neutron detection efficiency. This procedure was applied for both the experimental data and the Monte Carlo simulations. In the simulations a sample of events was generated with the $4NA_{(pppn)}$ and the $3NA^{L \geq 0}_{(ppp)n}$ phase space generators weighted according to the measured $4NA(pppn)$ and $3NA(ppp)$ cross sections. A comparison between the measured and simulated neutron detection efficiencies as a function of the kinetic energy and the polar angle is shown in Fig. 1. This comparison is after the application of an empirically determined overall scaling factor of 1.13 for the neutron detection efficiencies in the Monte Carlo to improve the agreement, because GEANT seems to underestimate these.

D. Classification of events

For the full decomposition of the $pppn$ final state of ^{4}He into absorption mechanisms a classification into certain event types turned out to be useful. The purpose was to produce separate distributions for the channels $(pp)pn$, $(ppp)n$, $(ppn)p$, and $(pppn)$ to get more constraints for the fits. These channels were approximated by the following classification scheme (note the use of square brackets to denote the experimental interpretation of the physics channels):

$$[pp]pn : T_{p1} > 20 \ \text{MeV}; T_{p2} > 20 \ \text{MeV}; T_{p3} \leqslant 20 \ \text{MeV}; T_n \leqslant 20 \ \text{MeV},$$

$$[ppp]n : T_{p1} > 20 \ \text{MeV}; T_{p2} > 20 \ \text{MeV}; T_{p3} > 20 \ \text{MeV}; T_n \leqslant 20 \ \text{MeV},$$

$$[ppn]p : T_{p1} > 20 \ \text{MeV}; T_{p2} > 20 \ \text{MeV}; T_{p3} \leqslant 20 \ \text{MeV}; T_n > 20 \ \text{MeV},$$

$$[pppn] : T_{p1} > 20 \ \text{MeV}; T_{p2} > 20 \ \text{MeV}; T_{p3} > 20 \ \text{MeV}; T_n > 20 \ \text{MeV}$$

The distributions presented in this paper (except the right-hand column of Fig. 4) will always be those with these thresholds on the laboratory kinetic energies T. To test the model dependence of the extrapolations of the cross sections down to zero threshold and their decompositions into mechanisms a data set with the same classification scheme, but a 30 MeV threshold, was also investigated. The variations in the results are reflected in the quoted uncertainties.

E. Fits and efficiency correction

Monte Carlo histograms for all event generators were produced in three different ways.

LADSON20: All simulated events were run through the analysis chain with the same cuts and resolutions as for the experimental data. Thus all losses caused by the detector (reactions in the scintillators, MWPC inefficiencies, geometrical acceptance, etc.) and the reconstruction software were reflected in these distributions. The above classification scheme with a 20 MeV threshold on the kinetic energy of the nucleons was applied; this rejected most of the 2NA events leaving predominantly those from 3NA and 4NA.

LADSOFF20: For these histograms the simulated data at the interaction vertex were used. With that, all distortions due to the detector and the reconstruction software were switched off, except the 20 MeV kinetic energy threshold. Again, all events were classified according to the scheme above.

LADSOFF0: These distributions were the simulated data at the interaction vertex as for LADSOFF20, but without the threshold requirements.

In the first step the LADSON20 distributions of all described event generators were simultaneously fit to the experimental data of the three channels $[ppp]n$, $[ppn]p$, and $[pppn]$, with the normalizations as free parameters. These fits were performed to various histogram sets: a set of histograms of the eight independent variables (β, γ, ξ, $\psi_{\min}$, $\psi_{\max}$, p_{p4}, ξ_{p4}, γ_{p4}), a set of two-dimensional histograms (triangular Dalitz plot, γ vs ξ), a set of one-dimensional histograms (momentum p_N, kinetic energy T_N, opening angles ψ_{NN}), a set of angle momentum correlations (Θ_p vs p_p, Θ_n vs p_n), and all of these sets together.

A critical generator was $2\text{NA}_{(pp)pn}$, with the pn pair unbound. The portion of the full isoscalar 2NA cross section ($\sigma_{2\text{NA}_{(pp)pn}}$ and $\sigma_{2\text{NA}_{(pp)d}}$) due to this process is very uncertain, but the fits usually indicated that it is small. This result is consistent with the finding of Ref. [30]. Therefore, all investigations discussed in this work were done with and without allowing a $2\text{NA}_{(pp)pn}$ contribution. This resulted in some spread of the multinucleon cross sections, which is the

main source for the uncertainties of the cross sections extrapolated to zero threshold.

In the second step the differential efficiencies $\eta_{ij}(x)$ for each simulated mechanism i, channel j, and variable x were determined according to

$$\eta_{ij}(x) = \frac{\text{LADSON20}_{ij}(x)}{\text{LADSOFF20}_{ij}(x)}. \tag{4.1}$$

Regions with $\eta_{ij}(x) < 1\%$ were removed. The efficiency corrected histograms were finally obtained with the formula

$$N(x) = \sum_i p_i \sum_j q_{ij} \frac{\Sigma_{k=1}^8 a_k N_{jk}(x)}{\eta_{ij}(x)} \tag{4.2}$$

with q_{ij} the fraction of events of mechanism i falling into channel j, p_i the normalization parameters from the fits, $N_{jk}(x)$ the histogram bin content per channel j and trigger type k of the experimental data, and a_k its corresponding prescale factor corrected for deadtime.

Each differential cross section presented in this paper was corrected binwise with this method. The average efficiency integrated over all events is of the order of 50% for the channels $[ppp]n$ and $[pppn]$, varying slightly with the incident pion energy; that of $[ppn]p$ is about 15%. Even when an extrapolation to zero threshold is made (LADSON20/ LADSOFF0) these average efficiencies remain of the order of 30% for $(ppp)n$ and $(pppn)$, and of 10% for $(ppn)p$.

The integrated cross sections cited in this paper for thresholds of 20 MeV and 30 MeV are mean values from the fits to the corresponding histogram sets with and without the $2\text{NA}_{(pp)pn}$ model. The error is taken to be the standard deviation of these fits. The partial cross sections for zero threshold are mean values of extrapolations from fits to all the various histogram sets with 20 MeV and 30 MeV thresholds. The error bars are the corresponding standard deviations of the results from the various fits. To test the model dependence of the results fits were also made with modified HFSI and ISI simulations, but the cross sections were usually inside the uncertainties obtained with the above-mentioned methods.

F. Normalization

The normalization of the differential and integrated cross sections was done in the same way as described in detail in Ref. [16]. The incident number of pions N_{beam} was corrected for the fraction which decay or react on their way from the beam defining counter to the target and for the number of pions which miss the target entirely. A correction was also made for the amount of contamination in the beam and the

efficiency of the beamline hodoscope. Where possible these correction factors were determined with the experimental data [27,28,43]. This gave the real number of pions N_π on the target. The number of target scatterers N_{scat} was calculated taking into account compression effects due to He being a nonideal gas at high pressure. The cross sections were calculated from the expression

$$\frac{d\sigma}{dx} = \frac{N(x)}{N_\pi \cdot N_{scat}}. \tag{4.3}$$

The normalization uncertainties include the systematic errors added in quadrature. The main sources of these errors are the uncertainties on the number of pions on the target, the number of target scatterers, background from the target walls, and on components of the acceptance correction such as reaction losses, particle identification, vertex reconstruction, and neutron efficiencies.

V. RESULTS

A. Signatures in differential distributions

1. ISI in the 3NA channels $(ppp)n$ and $(ppn)p$

In our semiclassical approach there are three different kinds of ISI that may contribute to the reaction $\pi^+{}^4\text{He} \rightarrow pppn$: The first, ISI($\pi^+p \rightarrow \pi^+p$)+2NA($\pi^+d \rightarrow pp$), leads to three energetic protons (ISI$_{(ppp)n}$) in the final state, with the neutron a spectator. The other two ISI mechanisms, ISI($\pi^+n \rightarrow \pi^+n$)+2NA($\pi^+d \rightarrow pp$) and ISI($\pi^+n \rightarrow \pi^0p$)+2NA($\pi^0d \rightarrow pn$), result in two protons and one neutron that are energetic (ISI$_{(ppn)p}$ and ISI$^{SCX}_{(ppn)p}$, respectively), with the third proton being a spectator. Evidence for signatures of ISI in the $3p$ multinucleon channel of ^{3}He and ^{4}He was discussed extensively in previous LADS publications [14,16]. In the following paragraphs we will investigate, for 239 MeV incident pion energy, whether there is also an ISI signature in the $(ppn)p$ channel of ^{4}He which was not investigated previously.

(a) ISI($\pi^+p \rightarrow \pi^+p$)+2NA($\pi^+d \rightarrow pp$): As the ''classical'' signature of this mechanism one expects one proton from the ISI process going into the forward hemisphere roughly following the quasifree πN kinematics, and a collinear proton pair from the 2N absorption that produces a peaklike structure in the laboratory opening angle spectrum of the proton pairs near 180° (shifted to lower values due to kinematic and phase space effects). Although the evidence for these signatures was discussed already in former LADS publications [14,16], they are shown again here for a direct comparison to the $[ppn]p$ channel. In Fig. 2 (left column) the signal of the forward scattered proton is visible in the data, and only the ISI$_{(ppp)n}$ simulation is able to approximately reproduce this feature. This signal is especially pronounced in the very forward hemisphere between 18° and 36° (see sliced projections) where the ISI simulation matches the data quite well. In other angular regions ISI appears to be less appropriate.

(b) ISI($\pi^+n \rightarrow \pi^+n$)+2NA($\pi^+d \rightarrow pp$): In this two-step mechanism the expected signatures are a forward scattered neutron with the πN kinematics from the ISI process, and a peaklike enhancement in the proton-proton laboratory open-

ing angle spectrum in the neighborhood of 180° from the 2N absorption. The neutron angle momentum correlation plot of Fig. 2 (middle column) again shows a distinct enhancement at the πN kinematics, similar to that in the $[ppp]n$ data. The ISI$_{(ppn)p}$ model gives a fair representation of the structure at forward angles (between 18° and 36°). At more backward angles additional strength (e.g., from ISI$^{SCX}_{(ppn)p}$) is necessary to match the data.

(c) ISI($\pi^+n \rightarrow \pi^0p$)+2NA($\pi^0d \rightarrow pn$): In this process one would expect a forward scattered proton with the πN kinematics, and a peak near 180° in the neutron-proton laboratory opening angle spectrum from the absorption of the π^0. The proton angle momentum correlation plot of Fig. 2 (right column) does not show a strong signal at the πN kinematics, but this signature could be masked by protons from the 2N absorption process of the ISI$^{SCX}_{(ppn)p}$ (and HFSI$_{(ppn)p}$) mechanism. The sliced projection of the forward hemisphere between 18° and 36° may indeed suggest some ISI from charge exchange, but there is more strength at higher momenta that cannot be accounted for by the ISI$^{SCX}_{(ppn)p}$ mechanism. At more backward angles both ISI(ppn) simulations are close to the data.

In summary, in the absorption of 239 MeV pions on ^{4}He we see evidence for the existence of all three ISI mechanisms, in particular in the forward angular regions. It even seems that the contribution of the ISI(ppn) mechanism (the sum of the middle and right columns of Fig. 2) is about as large as that of ISI(ppp), which is not expected from the isospin ratios for these reactions. In the data of 118 MeV (see Fig. 3), we see no explicit signatures of ISI, either in the $(ppp)n$ or the $(ppn)p$ channel.

The discussed evidence for an ISI signature in the laboratory opening angle data is shown in Fig. 4 for two different thresholds and compared to the distributions from the ISI and HFSI models. The $[ppp]n$ data show an enhancement at $\psi_{pp} \approx 150°$ which is in the same position as the peak suggested by the ISI$_{(ppp)n}$ simulation. This is less obvious in the $[ppn]p$ data. One could argue that the peak around 150° can also stem from HFSI. However, the distributions of both the experimental data and those of the ISI models are not very sensitive to the threshold. This is different for HFSI, where the bumps around 150° in the 20 MeV threshold data, a remnant of the 2NA step, are considerably reduced in the 30 MeV threshold spectra. From this threshold dependence one can conclude that HFSI cannot be the mechanism that causes the peak in the data, and moreover, that it is unlikely to be the main source of the 3NA yield at 239 MeV.

2. HFSI in the 3NA channels $(ppp)n$ and $(ppn)p$

We expect two types of two-step HFSI mechanisms that could be distinguishable in the data of the $pppn$ final state. The first one, 2NA($\pi^+d \rightarrow pp$)+HFSI($pp \rightarrow pp$), leads to three energetic protons in the final state (HFSI$_{(ppp)n}$) with the neutron being a spectator. The second process, 2NA($\pi^+d \rightarrow pp$) + HFSI($pn \rightarrow pn$), results in two protons and one neutron that are energetic (HFSI$_{(ppn)p}$); in this case one of the three protons acts as the spectator. In our previous investigations [14,16] we found that the evidence for a HFSI process in the $3p$ yield is weak, and difficult to identify. In the subsequent paragraphs we will look for a possible signa-
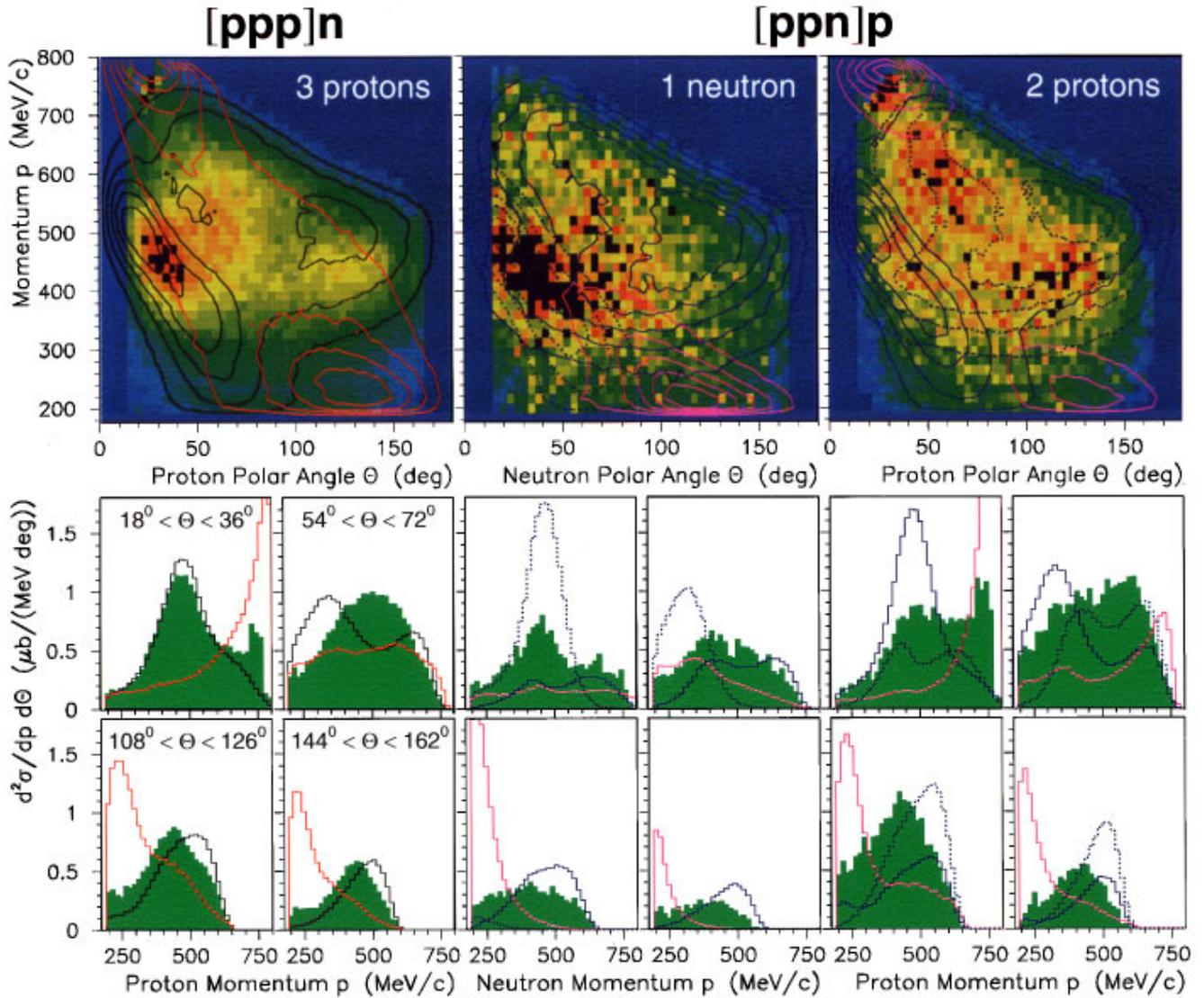
FIG. 2. (Color). θ_N vs p_N correlations (upper row) of the reaction $\pi^+ {}^4\mathrm{He} \to pppn$ at 239 MeV and sliced projections (lower rows) of the momentum p_N within selected angular regions. All histograms are corrected for acceptance. Each of the simulations is individually normalized to the full content of the two-dimensional histograms of the experimental data. The z axis of the two-dimensional plots is arbitrarily scaled; the color sequence is linearly increasing from blue, green, yellow, brown, to black. The four one-dimensional histograms below each correlation are momentum projections for the angular intervals $18° < \Theta_N < 36°$, $54° < \Theta_N < 72°$, $108° < \Theta_N < 126°$, and $144° < \Theta_N < 162°$. The green areas of the one-dimensional plots are the data corrected for acceptance. Left column: the three protons of the $[ppp]n$ channel compared to the $\mathrm{ISI}_{(ppp)n}$ (black line) and the $\mathrm{HFSI}_{(ppp)n}$ (red line) models. Middle column: the neutron of the $[ppn]p$ channel compared to the $\mathrm{ISI}_{(ppn)p}$ (dotted blue line), the $\mathrm{ISI}^{\mathrm{SCX}}_{(ppn)p}$ (solid blue line), and the $\mathrm{HFSI}_{(ppn)p}$ (pink line) models. Right column: the two fast protons of the $[ppn]p$ channel compared to the $\mathrm{ISI}^{\mathrm{SCX}}_{(ppn)p}$ (solid blue line), the $\mathrm{ISI}_{(ppn)p}$ (dotted blue line), and the $\mathrm{HFSI}_{(ppn)p}$ (pink line) models.

ture of HFSI in the $(ppn)p$ channel and compare it to $(ppp)n$; one expects $\mathrm{HFSI}(ppn) > \mathrm{HFSI}(ppp)$ because $\sigma_{pn} > \sigma_{pp}$. The pion energy of 118 MeV was chosen for this purpose, since there the contributions from ISI appear to be weak, while HFSI, if existent, may be important because of the energy dependence of the NN cross section.

(a) $2\mathrm{NA}(\pi^+ d \to pp) + \mathrm{HFSI}(pp \to pp)$: The elastic NN cross section decreases monotonically up to about 500 MeV incident nucleon energy. Because of this we expect the main distortions after the $2N$ absorption step on the backward going proton, while the higher energetic, forward proton should be less often disturbed. Therefore, if a HFSI process took place, we expect a signature of one high energetic forward

going proton and 2 low energetic (nonspectator) protons emerging in the backward hemisphere. Consistent with statements in our previous work, we find no clear evidence for the contribution of $\mathrm{HFSI}_{(ppp)n}$ strength in the $[ppp]n$ data of Fig. 3 (left column). Neither the proton angle momentum plot nor the sliced projections indicate the signatures discussed above. In particular, the forward angular region between 18° and 36° does not show the steep enhancement at high momenta suggested by the $\mathrm{HFSI}_{(ppp)n}$ simulation.

(b) $2\mathrm{NA}(\pi^+ d \to pp) + \mathrm{HFSI}(pn \to pn)$: From this two-step mechanism we expect a strong signal from an undisturbed 2NA proton at high momentum in the forward direction, and an enhanced yield in the proton and the neutron
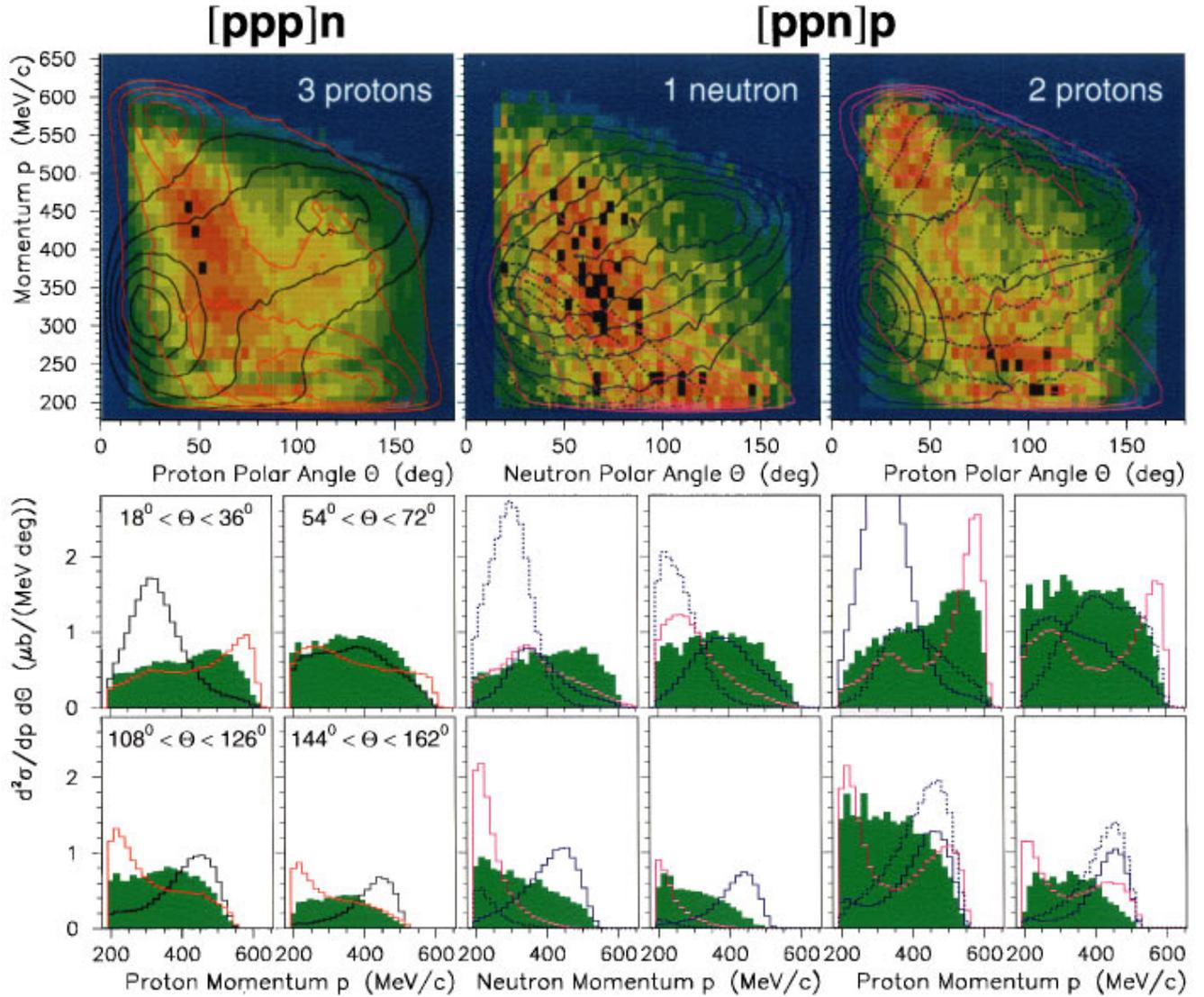
FIG. 3. (Color). θ_N vs p_N correlations (upper row) of the reaction π^+ ⁴He$\rightarrow pppn$ at 118 MeV and sliced projections (lower rows) of the momentum p_N within selected angular regions. The labels and color codes are the same as those of Fig. 2.

angle momentum correlation at momenta just above the particle threshold in the backward direction. In both the neutron spectrum of Fig. 3 (middle column) and the proton spectrum of Fig. 3 (right column) such a feature appears to be indicated. Although not as pronounced as suggested by the HFSI$_{(ppn)p}$ model, the sliced projection between 18° and 36° of the proton spectra (right column) confirms this enhancement in the $[ppn]p$ data at high momenta. Also the backward angle slices of the neutron spectra tend to show some evidence for an enhancement at low momenta. However, these potential signatures of a HFSI mechanism can only account for a minor fraction of the $(ppn)p$ yield.

In summary, there may be evidence for a weak HFSI signal in pion absorption at 118 MeV on ⁴He that feeds the $(ppn)p$ channel. However, the signals suggested by the HFSI models seem to be less distinct in the data. Moreover, the data show yield in regions that cannot be populated strongly by our cascade HFSI (or ISI) mechanisms. At the higher energy of 239 MeV (see Fig. 2) there is no evidence for a contribution from the HFSI mechanisms.

3. SFSI signatures in 3NA Dalitz plots

In Ref. [16] we showed that it is important to take into account a SFSI (soft final state interaction) in the simulations in order to reproduce some distributions correctly, although it proved difficult to quantify this effect in the $3p$ yield reliably. The situation is different for the $(ppn)p$ channel, since the SFSI yield from the pn interaction is much larger than that from the pp interaction. Then if we use a histogram where the yield from SFSI is well concentrated in a certain region, we can simply take the difference between the distributions of the $(ppn)p$ and $(ppp)n$ channels to obtain a fair approximation of the SFSI component in the former.

The distribution that fulfills the above requirement is the triangular Dalitz plot (for a more detailed discussion see Ref. [16]). Its strong correlation to angular configurations of the three particles considered makes it almost ideal to identify SFSI in the 3NA yield. In Fig. 5 the Dalitz plots for the $[ppp]n$ and the $[ppn]p$ channels are compared. For the $[ppn]p$ channel both fast protons and the neutron were re-
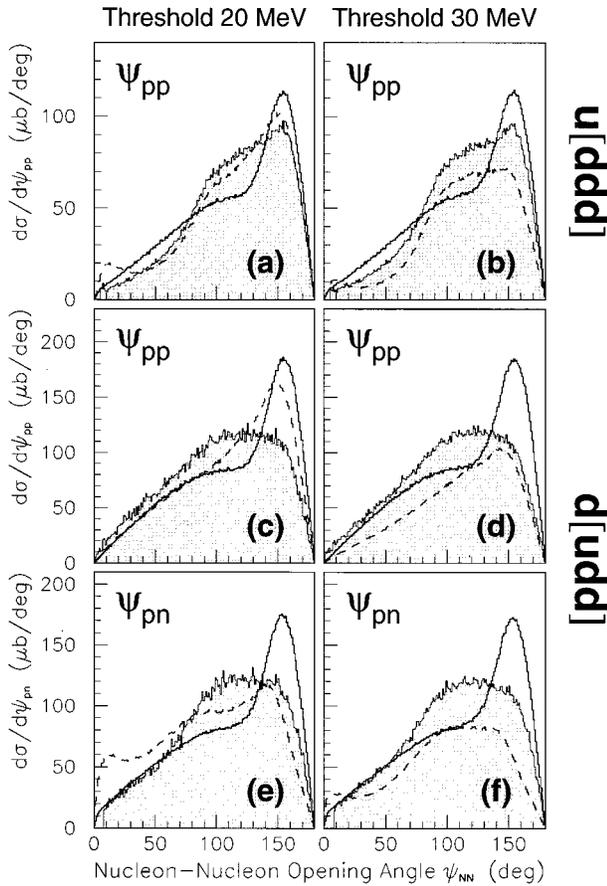
FIG. 4. Nucleon-nucleon laboratory opening angles ψ_{NN} of the reaction $\pi^{+4}\mathrm{He}\rightarrow pppn$ at 239 MeV. Left column [(a),(c),(e)]: $T_{N1-N3}>20$ MeV; $T_{N4}\leqslant 20$ MeV. Right column [(b),(d),(f)]: $T_{N1-N3}>30$ MeV; $T_{N4}\leqslant 30$ MeV. The shaded areas are the acceptance corrected data, and the dashed and solid lines the results of HFSI and ISI simulations, respectively, normalized to the yield with the 20 MeV threshold; the results of the simulations for the 30 MeV data retain this normalization but with the higher threshold applied. (a)+(b): ψ_{pp} of the $[ppp]n$ channel (all three combinations added) compared to the $\mathrm{ISI}_{(ppp)n}$ and the $\mathrm{HFSI}_{(ppp)n}$ models. (c)+(d): ψ_{pp} of the $[ppn]p$ channel (all three combinations added) compared to the $\mathrm{ISI}_{(ppn)p}$ and the $\mathrm{HFSI}_{(ppn)p}$ models. (e)+(f): ψ_{pn} of the $[ppn]p$ channel (all three combinations added) compared to the $\mathrm{ISI}^{SCX}_{(ppn)p}$ and the $\mathrm{HFSI}_{(ppn)p}$ models.

garded as indistinguishable particles to treat them in the same way as the three protons from $[ppp]n$. The most striking differences of the two plots are the three pronounced peaks in the $[ppn]p$ channel. These are in the positions of two parallel particles of similar energy, and thus reflect the yield from pn SFSI.

Since the rest of the Dalitz plot is rather similar for both 3NA channels, we may normalize the central region of $[ppp]n$ to that of $[ppn]p$ and take the difference between the two distributions. The remaining strength in the peaks gives a rough estimate of the SFSI yield in the 3NA channels (neglecting pp SFSI because it is much weaker). For the 20 MeV threshold data we find a SFSI yield in the 3NA(ppn) channel of 5%, 4%, 3%, 2%, and 1% of the total strength for the pion energies 70, 118, 162, 239, and 330 MeV, respectively.
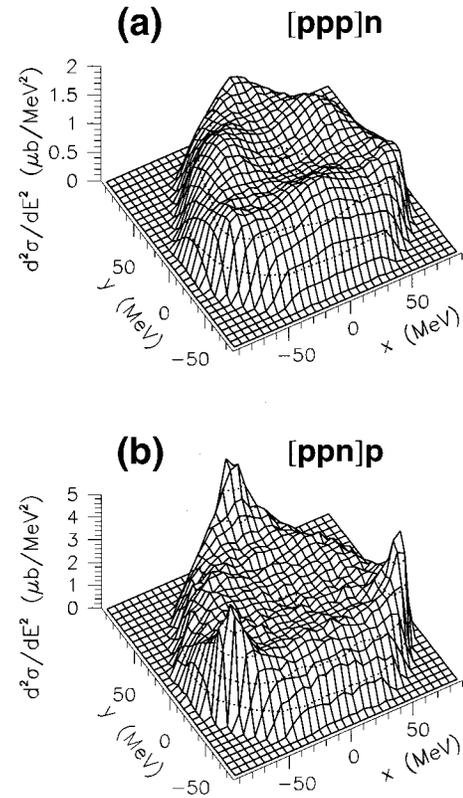

FIG. 5. Triangular Dalitz plots of 3NA on $^4\mathrm{He}$ for the channels $[ppp]n$ (a) and $[ppn]p$ (b). The incident pion energy was 162 MeV. The sharp peaks in the $[ppn]p$ channel are due to pn SFSI. The variables are defined as $x=(T_1-T_2)/\sqrt{3}$ and $y=T_3-Q/3$, with $Q=T_1+T_2+T_3$ and T_i the kinetic energy of the nucleon i in the 3N c.m. system.

4. 4NA in the (pppn) channel

With the assumption of 2NA being the basic pion absorption process, if there is no coherent 3NA or 4NA process and if the contributions from high momentum tails of spectator nucleons are small, a final state with four energetic nucleons (4NA) can only be formed by a three-step process. Such a three-step mechanism could be composed of three simple interaction sequences: (ISI+ISI+2NA), (ISI+2NA+FSI), and (2NA+FSI+FSI). While the latter 4NA mechanism is probably very hard to identify (there are already problems with 2NA+FSI), the first two processes should still carry some signature of the forward scattered nucleon from the initial ISI step.

In Fig. 6 the proton and neutron momentum spectra of the forward hemisphere between 18° and 36° of the $[pppn]$ channel are compared for all five pion energies. In the proton spectra at higher energies ($\geqslant$ 162 MeV) we find a peaklike structure at the quasifree πN kinematics, which is indicated by the arrow. These structures may suggest that the three-step processes (ISI+ISI+2NA) and/or (ISI+2NA+FSI) are seen in the 4NA data. On the other hand, a process like (ISI+3NA) would also lead to such a signature, so that the existence of a coherent 3NA process is not excluded by the forward scattering signal in the 4NA data.

An attempt was made to find signatures of the potential ''double-Δ'' mechanism ($\Delta\Delta$) in the 4NA data. This mechanism should lead to peaks around 165° in both the pp and
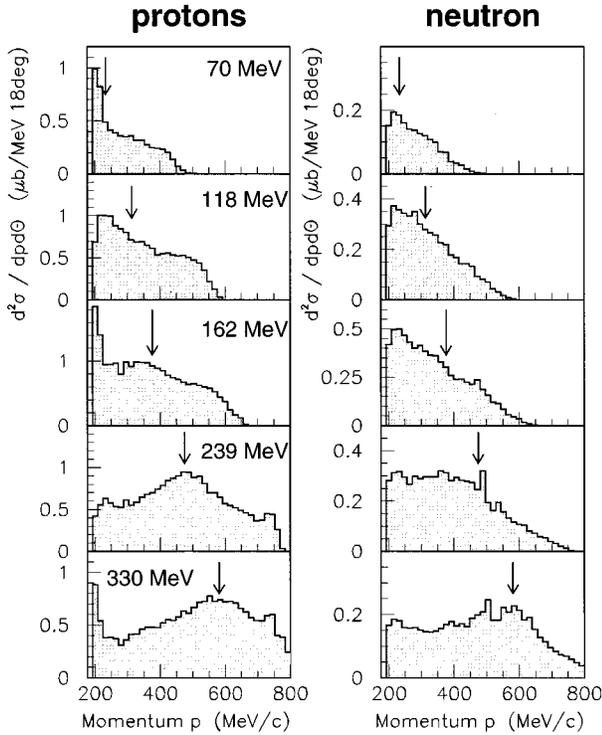
FIG. 6. Proton (left) and neutron (right) momentum yields of the pion absorption channel $[pppn]$ (for definition see Sec. IV D) on ^{4}He within an angular region of $18°$–$36°$ for the five incident pion energies 70, 118, 162, 239, and 330 MeV. Always all three protons in the given range are plotted in the left histograms. The arrows indicate the positions of a nucleon in quasifree πN kinematics.

pn laboratory opening angle spectra, since the $\Delta\Delta$ would decay with the same signatures as two 2NA processes. No such peaks are apparent in our 4NA data. Therefore, to enhance a possible $\Delta\Delta$ signal the 4NA data were analyzed with the requirement of two back-to-back nucleon pairs ($150° < \psi_{NN}^{lab} < 180°$) of about equal momentum in the $4N$ c.m. frame. The fractions of data events (f_{data}) fulfilling these cuts were compared to the ones (f_{MC}) for the $4NA_{(pppn)}$ phase space simulation. For the $[pppn]$ channel as defined in Sec. IV D we find the ratios $f_{data}/f_{MC} = 1.5$, 1.0, 1.2, 1.1, and 1.0 for 70, 118, 162, 239, and 330 MeV, respectively, which shows almost no energy dependence. This is in contradiction to the predicted increase [22] in the $\Delta\Delta$ cross sections over these energies of about a factor of 25. Further, as the incident pion energy increases, any such back-to-back signal should tend to become clearer due to less kinematic smearing. Thus there appears to be no evidence for a "double-Δ" mechanism in our 4NA data.

5. Summary

We have shown here that kinematic signatures of ISI and HFSI may be identified in both the $[ppp]n$ and $[ppn]p$ 3NA distributions, with the ISI being more pronounced at the higher pion energies and HFSI at the lower. SFSI has also been identified and quantified in the $[ppn]p$ Dalitz plot. The 4NA yield is substantially above that expected from the tails of 3NA mechanisms and contains an apparent ISI signature; the data do not provide evidence for a significant contribution from the "double-Δ" mechanism.

B. Differential cross sections

In this section the acceptance corrected differential distributions over the eight independent variables will be shown for the five incident pion energies and the three channels $[ppp]n$, $[ppn]p$ and $[pppn]$, as defined in Sec. IV D. These distributions are intended to give cross sections for a complete set of variables and to show the quality of the fits of the 10 (or 11 if tails from 2NA are included) models to the data for the four-nucleon final state $pppn$. The data will be compared to the summed contributions of the fitted models; to keep the figures managable, the individual distributions of the simulations are not included.

1. Azimuthal angle β

Since this experiment is not sensitive to polarization observables, the measured cross sections should be symmetric in a rotation around the beam axis. The azimuthal angle β reflects such a rotation of the c.m. plane, spanned by three out of the four final state particles of $pppn$, and should give structureless distributions. That this is well fulfilled was shown in Ref. [16] (Fig. 11) and was found to be the case also in this analysis for all five energies and the three channels $[ppp]n$, $[ppn]p$, and $[pppn]$.

2. Plane angle ξ

In Ref. [16] we found that the distributions of the plane angle ξ show an indication that angular momentum components of up to at least $L = 2$ are necessary to describe the data properly. This finding was valid for the (ppp) channel of both ^{3}He and ^{4}He and is consistent with a strong coupling of this multinucleon absorption channel to $\pi N \rightarrow \Delta$ vertices. In this analysis we have similarly fitted a parametrization of ξ in terms of an expansion into Legendre polynomials to the (ppn) data:

$$\frac{d\sigma}{d\Omega_\xi} = \frac{d^2\sigma}{d\beta \, d\cos\xi} = \sum_{n=0}^{L} A_{2n} P_{2n}(\cos\xi). \qquad (5.1)$$

Fits of this expansion to the data result in the Legendre coefficients A_0, A_2, and A_4, which are given in Table II for the $[ppp]n$ and the $[ppn]p$ channels in ^{4}He. Note that the numbers for the $[ppp]n$ channel are slightly different from those of Ref. [16] because of the different thresholds used when fitting the results.

The ratios A_2/A_0 and A_4/A_0 are also given in Table II and plotted in Fig. 7. As a notable result we find very different slopes for these ratios for the channels $[ppp]n$ and $[ppn]p$. While there is a clear energy dependence in the $[ppp]n$ channel, the ratios of the $[ppn]p$ channel seem to be basically constant with energy, but also show an $L=1$ angular momentum contribution. The same ratios evaluated for the ISI(ppp), ISI(ppn), HFSI(ppp), and HFSI(ppn) models do not show a trend clearly enough to allow conclusions to be drawn about different strengths of ISI and HFSI in the $[ppp]n$ and $[ppn]p$ channels. It may also be interesting to note that the sums of A_2/A_0 and A_4/A_0 are about -0.5 for both channels independent of the incident pion energy.

In Fig. 8 the acceptance corrected distributions over ξ are shown for the five energies and three channels. The data are

TABLE II. 3NA Legendre coefficients for the ^{4}He absorption channels $[ppp]n$, $[ppn]p$ (for definition see Sec. IV D) for an angular momentum content of the final state of $L \leq 2$. The first uncertainties are the errors from the fits, the second on A_0 reflect the normalization uncertainties. The error on the coefficient ratios contain both uncertainties.

Channel	T_π (MeV)	$A_0\left(\dfrac{\mu b}{sr}\right)$	$A_2\left(\dfrac{\mu b}{sr}\right)$	$A_4\left(\dfrac{\mu b}{sr}\right)$	$\dfrac{A_2}{A_0}$	$\dfrac{A_4}{A_0}$
	70	$156 \pm 11 \pm 25$	-62 ± 4	-10 ± 4	-0.40 ± 0.08	-0.07 ± 0.03
	118	$362 \pm 16 \pm 29$	-126 ± 7	-52 ± 6	-0.35 ± 0.04	-0.14 ± 0.02
$[ppp]n$	162	$561 \pm 27 \pm 56$	-251 ± 12	-37 ± 10	-0.45 ± 0.05	-0.07 ± 0.02
	239	$461 \pm 24 \pm 37$	-323 ± 12	54 ± 9	-0.70 ± 0.07	0.12 ± 0.02
	330	$304 \pm 14 \pm 30$	-257 ± 6	90 ± 5	-0.85 ± 0.10	0.30 ± 0.04
	70	$627 \pm 63 \pm 100$	-258 ± 41	20 ± 21	-0.41 ± 0.10	0.03 ± 0.03
	118	$949 \pm 62 \pm 76$	-369 ± 33	-12 ± 21	-0.39 ± 0.05	-0.01 ± 0.02
$[ppn]p$	162	$1294 \pm 64 \pm 129$	-627 ± 25	73 ± 19	-0.48 ± 0.06	0.06 ± 0.02
	239	$719 \pm 120 \pm 57$	-356 ± 9	10 ± 11	-0.50 ± 0.09	0.01 ± 0.02
	330	$692 \pm 148 \pm 69$	-372 ± 21	109 ± 19	-0.54 ± 0.13	0.16 ± 0.05

reasonably well reproduced by the fits of the simulated model distributions. Note that these fits are to the full set of histograms, not just to the single variable Legendre polynomial fits discussed above.

3. Rotation angle γ

In Ref. [16] we discussed the sensitivity of the rotation angle γ to the reaction mechanisms. We can also use this sensitivity to look for different magnitudes of ISI and HFSI in the $[ppp]n$ and $[ppn]p$ channels, since we know from our earlier work ([16], Fig. 15) that these mechanisms popu-

FIG. 7. Coefficient ratios A_2/A_0 (a) and A_4/A_0 (b) of the fits of Legendre polynomials [Eq. (5.1)] to the plane angle ξ for the $[ppp]n$ (solid dots) and the $[ppn]p$ (open squares) channels with a 20 MeV threshold.

late different regions in the γ distributions of $[ppp]n$ (around $|\gamma| = 0°$ for ISI and around $\gamma = 100°$ for HFSI). These arguments remain the same for the γ distributions of $[ppn]p$ shown in this paper.

The γ distributions (Fig. 9) of $[ppp]n$ and $[ppn]p$ are indeed rather different. The peaklike structures around $|\gamma| = 0°$ at higher incident pion energies in the $[ppp]n$ channel are less pronounced in the $[ppn]p$ one. On the other hand, there is significant strength around $\gamma = 100°$ in the $[ppn]p$ distributions. These findings suggest that compared to ISI the HFSI mechanism may be relatively more important in the $[ppn]p$ channel than in the $[ppp]n$ one. This will be confirmed by the results in Sec. V C 1. As found in Ref. [16], the models do not reproduce the data well, especially in the middle part of the $[ppp]n$ spectra. Although less pronounced in the $[ppn]p$ channel there are discrepancies in these spectra as well.

At this point we should also note that the discrepancies are correlated to the bumps in the $[ppp]n$ Dalitz plot, near, e.g., $(x,y) = (0,-50)$ in Fig. 5(a), which were found to be unexplainable with simple cascade models in Ref. [16]. Such bumps are also visible in the Dalitz plot of the $[ppn]p$ channel [Fig. 5(b)], though they may be less pronounced there. In Ref. [16] it was suggested that the structures in the $[ppp]n$ channel might be due to interference effects not contained in the semiclassical cascade models; such effects could appear differently in the $[ppn]p$ channel because of the other isospin.

In the $[pppn]$ channel the fits reproduce the data relatively well at all energies. However, there are again some structures in the central region of the histograms at higher pion energies that could stem from the same mechanisms as those in the $[ppp]n$ channel.
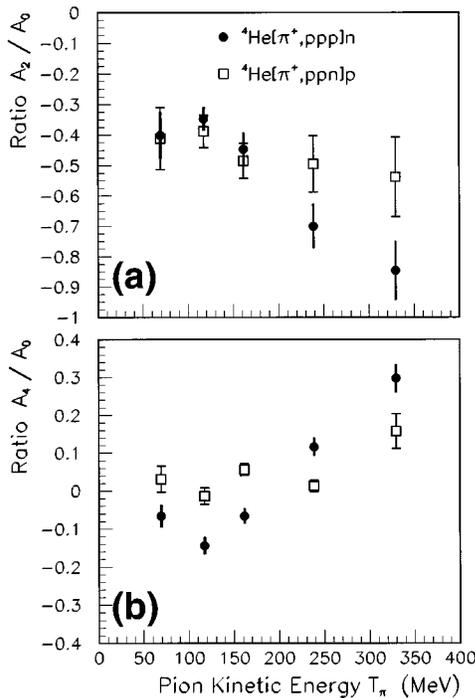
4. Minimum opening angle ψ_{min} and maximum opening angle ψ_{max}

In Fig. 10 and Fig. 11 the spectra of the minimum and maximum opening angles, ψ_{min} and ψ_{max}, respectively, are compared for the channels $[ppp]n$, $[ppn]p$, and $[pppn]$ at the different incident pion energies. These variables appear
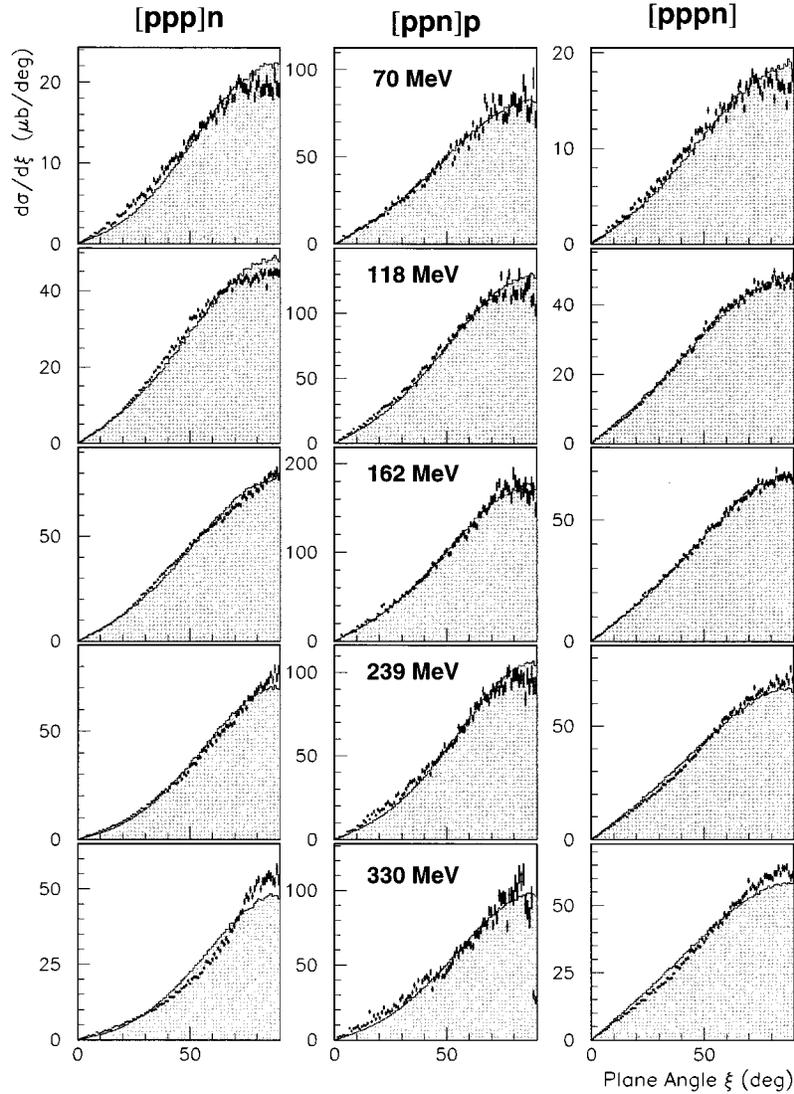
FIG. 8. Distributions over the plane angle ξ for the reaction π^{+4}He$\rightarrow pppn$ for incident pion energies of 70, 118, 162, 239, and 330 MeV (from the top) with a threshold of 20 MeV. The data are the dots with error bars, the fitted sums of the simulations are the shaded areas. The columns show the channels $[ppp]n$ (left), $[ppn]p$ (middle), and $[pppn]$ (right). Normalization uncertainties are not included in the error bars.

to be quite structureless and in most cases the data are well reproduced by the fitted models. The strength down to $\psi_{min}=0°$ or up to $\psi_{max}=180°$ is a reflection of soft final state interactions (see also Ref. [16]). The effect is visible most clearly in the $[pppn]$ spectra, since in these data the probability of a pn pair with similar momentum is quite high.

5. Fourth-particle momentum p_{p4}

In the channels $[ppp]n$ and $[ppn]p$ the data of the momentum distributions p_{p4} of the fourth particle (Fig. 12) are well reproduced by the simulations. These spectra mainly reflect the Fermi motion of the spectator nucleon in the 3NA channels and indicate that the one-nucleon momentum distribution chosen for the simulations is close to the real one. For the $[pppn]$ channel the simulations are also a good representation of the data. Recall that p_{p4} is the momentum of the lowest energy nucleon in the laboratory, calculated in the c.m. system of the other nucleons, while the threshold cut is

applied in the lab frame. This explains the variation of the distributions' end points with the incident pion energy.

6. Angle ξ_{p4}

The angle ξ_{p4} reflects how close the fourth particle's momentum vector lies to the c.m. plane of the three other nucleons, with a value of 90° indicating that the momentum of the fourth particle is also in this plane. Hence this variable should be especially sensitive to SFSI effects. If the fourth particle's momentum vector lies in the c.m. plane, the probability of nucleon pairs with similar momenta is high, and one would expect to find a signal around $\xi_{p4}=90°$. This signature is indicated in all spectra of Fig. 13. It is suppressed in the $[ppp]n$ and $[ppn]p$ channels, since the fourth nucleon is always below the 20 MeV kinetic energy threshold. The situation is different in the $[pppn]$ channel where all four particles are above 20 MeV, and can have similar momentum. The effect is the peak at $\xi_{p4}=90°$. The quality of the fits shows in addition that SFSI is correctly taken into
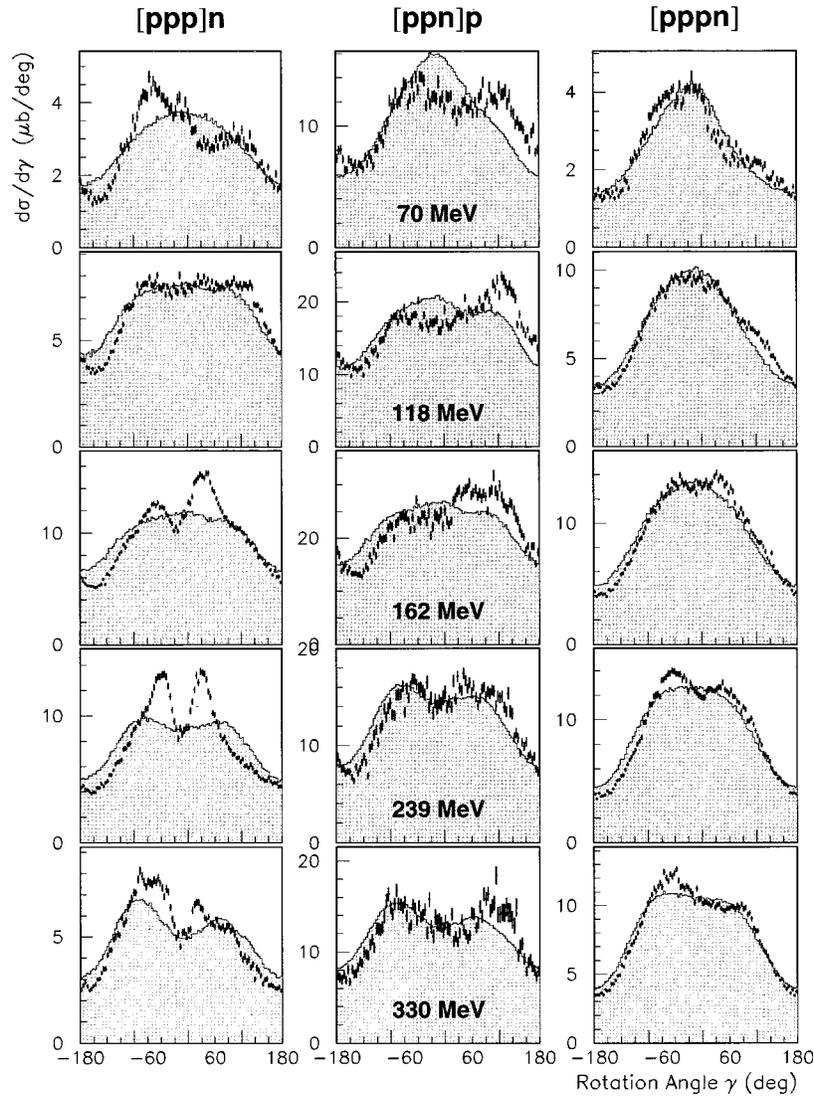
FIG. 9. Distributions over the rotation angle γ for the reaction $\pi^{+4}\text{He} \to pppn$ for incident pion energies of 70, 118, 162, 239, and 330 MeV (from the top) with a threshold of 20 MeV. For further information see Fig. 8.

account in the models, because not including the SFSI in the simulations would give no sharp peak at $\xi_{p4} = 90°$. With an integration of this peak we can evaluate a rough estimate of the amount of SFSI in the $[pppn]$ channel. We find that for the five (increasing) incident pion energies 11%, 8%, 7%, 4%, and 3% of the yield in this channel include a SFSI.

It should be noted that the SFSI seen in this variable is a reflection of the interaction between the fourth (slowest) particle and one of the three plane nucleons. This has to be clearly distinguished from the SFSI discussed in Sec. V A 3, which reflects this type of interaction between the three plane nucleons. If we add both contributions from 3NA(ppn) and 4NA($pppn$) weighted by their actual cross section we get the result that at pion energies of 70, 118, 162, 239, and 330 MeV about 5.1%, 3.5%, 3.0%, 2.0%, and 1.8%, respectively, of the total $pppn$ multinucleon absorption yield with at least three nucleons above 20 MeV includes a SFSI.

7. Rotation angle γ_{p4}

The distributions of the rotation angle γ_{p4} shown in Fig. 14 are very similar in the $[ppp]n$ and $[ppn]p$ channels. The

strong dependence of the shape of the distributions on the incident pion energy is a reflection of the increasing total energy in the absorbing system. The least energetic nucleon is forced to be below 20 MeV: therefore, the total energy is fully absorbed in the 3N system which gets a strong boost forwards, and the spectator nucleon has to go backward (or to around 180° in γ_{p4}). This is not the case in the $[pppn]$ channel: then the fourth particle can also go forward, leading to a flatter distribution especially at the low incident pion energies. The fits are in good agreement with the data.

8. Summary

The comparisons of the fits with the data of Figs. 8–14 show that the overall agreement of the fits with the data is good, but that there are significant detailed deviations (e.g., in the rotation angle distributions and the Dalitz plots), especially in the $[ppp]n$ and $[ppn]p$ channels. Thus although the signatures of ISI, HFSI, and SFSI discussed in Sec. V A suggest strongly that these processes occur, the deviations from the fits also suggest that dynamical details or strong interference effects lacking in our models may be significant.
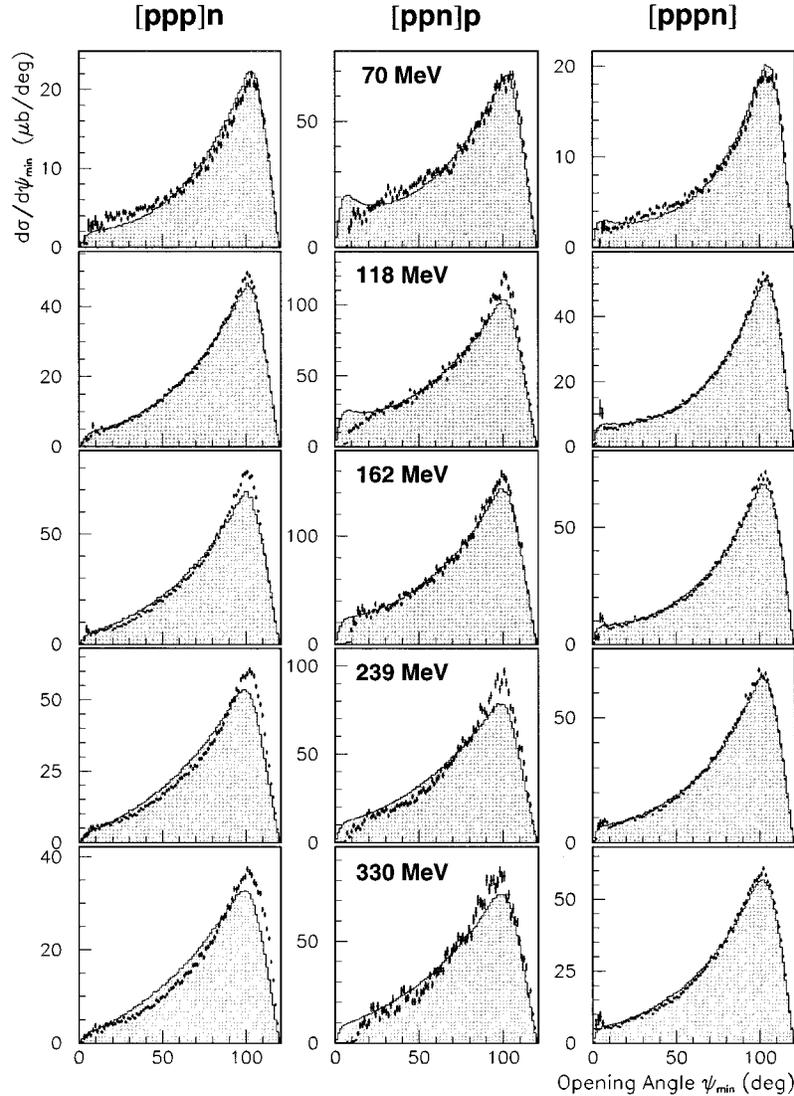
FIG. 10. Distributions over the minimum opening angle ψ_{min} for the reaction $\pi^+{}^4$He$\rightarrow pppn$ for incident pion energies of 70, 118, 162, 239, and 330 MeV (from the top) with a threshold of 20 MeV. For further information see Fig. 8.

The phase-space-like components of the distributions demonstrate nonzero orbital angular momentum content.

C. Fractional decomposition into mechanisms and integrated cross sections

1. Decomposition into mechanisms

In Sec. V A we showed that the data contain various qualitative signatures of some reaction mechanisms, and in this section we quantify their importance in terms of our simple (ISI+2NA) and (2NA+HFSI) cascade models. In Refs. [14,16] we found that a significant fraction of the three-proton cross section on ^{3}He around and especially above the Δ resonance can be accounted for by an ISI mechanism followed by 2NA. Quantitatively this means that on ^{3}He, with increasing pion energy, between 3% and 13% of the total absorption cross section, or 14–33% of the 3NA yield, was found to be attributable to such a two-step process. Although more suppressed at lower incident pion energies, a roughly comparable fraction of ISI was found in the 3p yield on ^{4}He.

Both in Ref. [14] and Ref. [16] it was stated that a possible contribution of a HFSI mechanism cannot be easily distinguished from a 3N phase space distribution, but it was also observed that the HFSI yield leading to three energetic protons usually seemed to be smaller than the ISI yield. More than half of the 3p yield was found to be not explainable by simple cascade processes both in ^{3}He and ^{4}He.

In this work a decomposition of the full multinucleon final state $pppn$ of ^{4}He was done with a simultaneous fit of 10 (or 11 when 2NA was included) models to the distributions of the data. The results, extrapolated to zero threshold, are given in Table III. Although the uncertainties of most of the fractions are rather large, the results show some trends in the energy dependences of the various mechanisms. The percentages and uncertainties given in Table III are averages and standard deviations, respectively, of the results of altogether 20 fits with different variable sets and thresholds, with and without allowing a 2NA tail. The main results of Table III are repeated in Table IV, as a fraction of the total absorption cross sections on ^{4}He which were taken from Ref. [30].

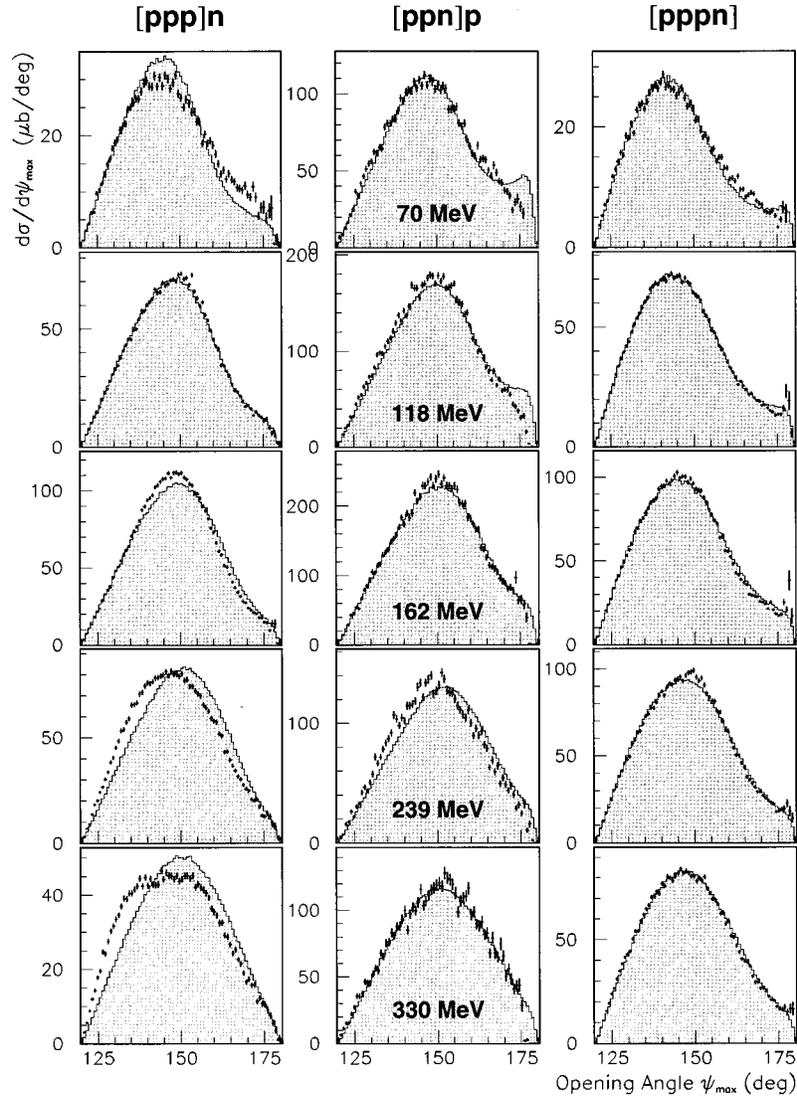The results for the ISI mechanism leading to three energetic protons [ISI(ppp)] are in good agreement with the

FIG. 11. Distributions over the maximum opening angle $\psi_{\max}$ for the reaction $\pi^+ {}^4\text{He} \to pppn$ for incident pion energies of 70, 118, 162, 239, and 330 MeV (from the top) with a threshold of 20 MeV. For further information see Fig. 8.

cross sections obtained with the method used in Ref. [16]. Surprisingly, the contribution of the ISI(ppn) mechanism comes out significantly larger than one would expect by simple isospin arguments. In this case the fractions from the two ISI(ppn) mechanisms were added because their individual numbers have large correlated uncertainties. The actual average values from the fits are given here for completeness for the pion energies 70, 118, 162, 239, and 330 MeV: ISI$_{(ppn)p}$: 2±4%, 0±1%, 1±2%, 5±3%, and 7±6%; ISI$^{SCX}_{(ppn)p}$: 7±9%, 3±3%, 3±3%, 11±4%, and 6±5%. The uncertainties for ΣISI$_{(ppn)p}$ in Table III are considerably smaller because the two individual ISI(ppn) fractions were always added before the averaging of the fit results was done. From the summed fractions of the three fitted ISI processes we conclude that the contribution of the (ISI+2NA) mechanism to the multinucleon strength in ^{4}He increases with the incident pion energy. This trend one would expect from simple consideration of the quasifree πN and 2NA cross sections. The fractions of total ISI leading to final states with three energetic particles varies with energy from around 3% to 11% (Table IV) and is comparable to the results found for ^{3}He [16].

The fractions found for the HFSI mechanisms indicate that the yield of the HFSI(ppn) process is significantly stronger than that of the HFSI(ppp) process. The observed ratio is roughly in agreement with what one would expect from the elastic pn and pp cross sections. Also the trend of decreasing importance of HFSI with increasing pion energy is to be expected from the behavior of the NN cross sections. At lower pion momenta the average kinetic energy per nucleon after the absorption process is smaller and the probability of a nucleon rescattering in the final state is bigger. In comparison to the total pion absorption cross section on ^{4}He [30] the HFSI contribution can be evaluated to be about 8% at 70 MeV, while above the Δ resonance it appears to be negligible (Table IV). It should be noted that effects from SFSI (see Sec. V B 6) are not included in these HFSI numbers. The possible FSI yields leading to deuteronic final states are also not taken into account in this analysis.

Although ISI and for the first time also HFSI have been identified in the $pppn$ multinucleon absorption final state of ^{4}He, only about 25% (possibly a bit more at 70 MeV) of the yield can be accounted for by our semiclassical cascade
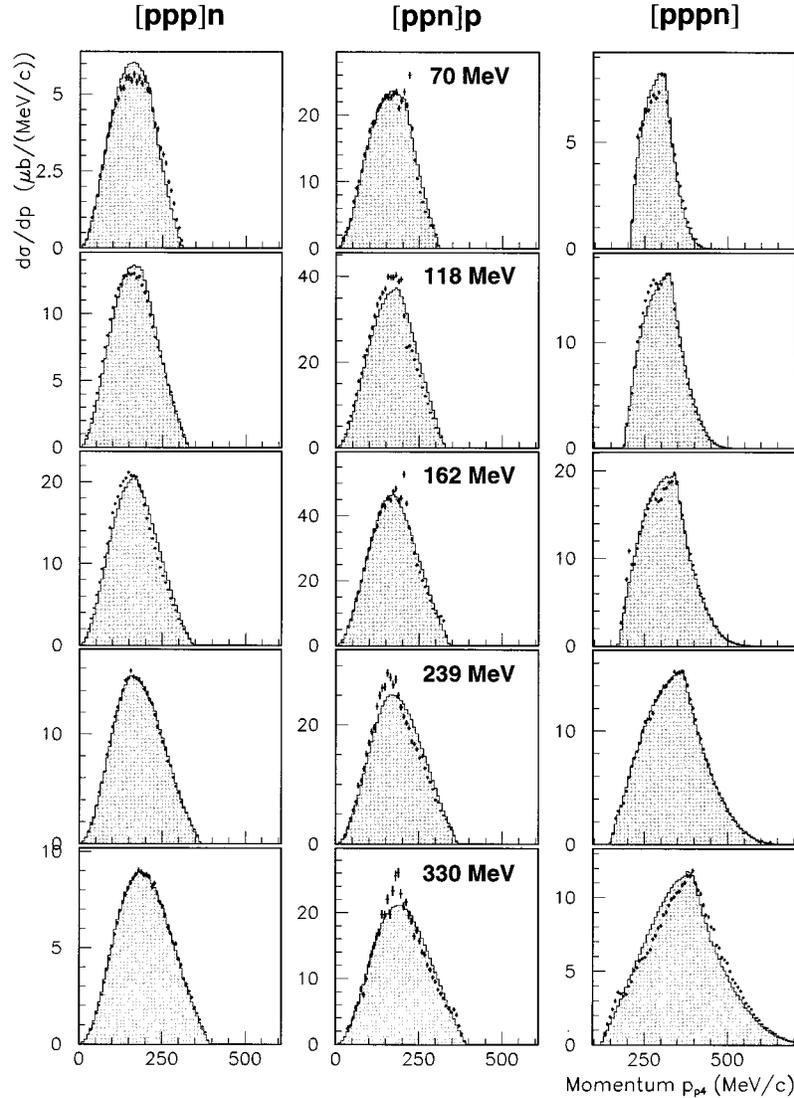
FIG. 12. Distributions over the momentum p_{p4} of the fourth particle in the c.m. system of the other three nucleons for the reaction $\pi^+{}^4\text{He} \rightarrow pppn$ for incident pion energies of 70, 118, 162, 239, and 330 MeV (from the top) with a threshold of 20 MeV. For further information see Fig. 8.

models. The remainder is well fitted by simple phase space distributions, if angular momentum components up to p-wave are taken into account.

For the 3N-PS(ppn) yield a rough trend is visible of the constant term ($L \geq 0$) being more important at lower incident pion energies and contributions from $L \geq 1$ being dominant at the higher ones. The correlation matrix of the fits suggests that the very low fraction of 3NA$^{L \geq 0}_{(ppn)p}$, and thus the low fraction of 3N-PS(ppn), at 239 MeV is probably caused by a strong correlation of this model and the ISI$^{\text{SCX}}_{(ppn)p}$ distributions, which also would explain the rather high fraction of the ISI$^{\text{SCX}}_{(ppn)p}$ mechanism at this energy. Taking this into account, the fractions of the total 3N-PS(ppn) yield show little energy dependence.

While the $L \geq 1$ contribution also seems to increase with the pion energy in the 3N-PS(ppp) yield, the trend in this channel appears different for the $L \geq 0$ fractions which first increase and then decrease in energy. A possible explanation for this behavior could be a loss of 3NA(ppp) strength into the deuteronic final state ppd at the lower energies. One

would expect this effect to be more pronounced in the 3NA (ppp) channel than in 3NA(ppn) because of nucleon counting arguments. This may also contribute to the 3N-PS(ppn) yield being larger than that for 3N-PS(ppp) by a factor ranging from about 3 to 1.5, as the incident pion energy increases.

The contribution of a 4N-PS($pppn$) mechanism to the $pppn$ multinucleon final state is increasing with the incident pion energy. Compared to the total pion absorption cross section on ^{4}He we find a fraction of 1% to 8% between 70 and 239 MeV (Table IV).

2. Cross sections

In Table V the cross sections of multinucleon pion absorption on ^{4}He into the $pppn$ final state are summarized. Also given are the decompositions of the yields into the 3NA channels $(ppp)n$ and $(ppn)p$, and the 4NA channel $(pppn)$. The cross sections are average values gained from 20 fits to the distributions of various variable sets with different thresholds, with and without a 2NA tail. Fits were also
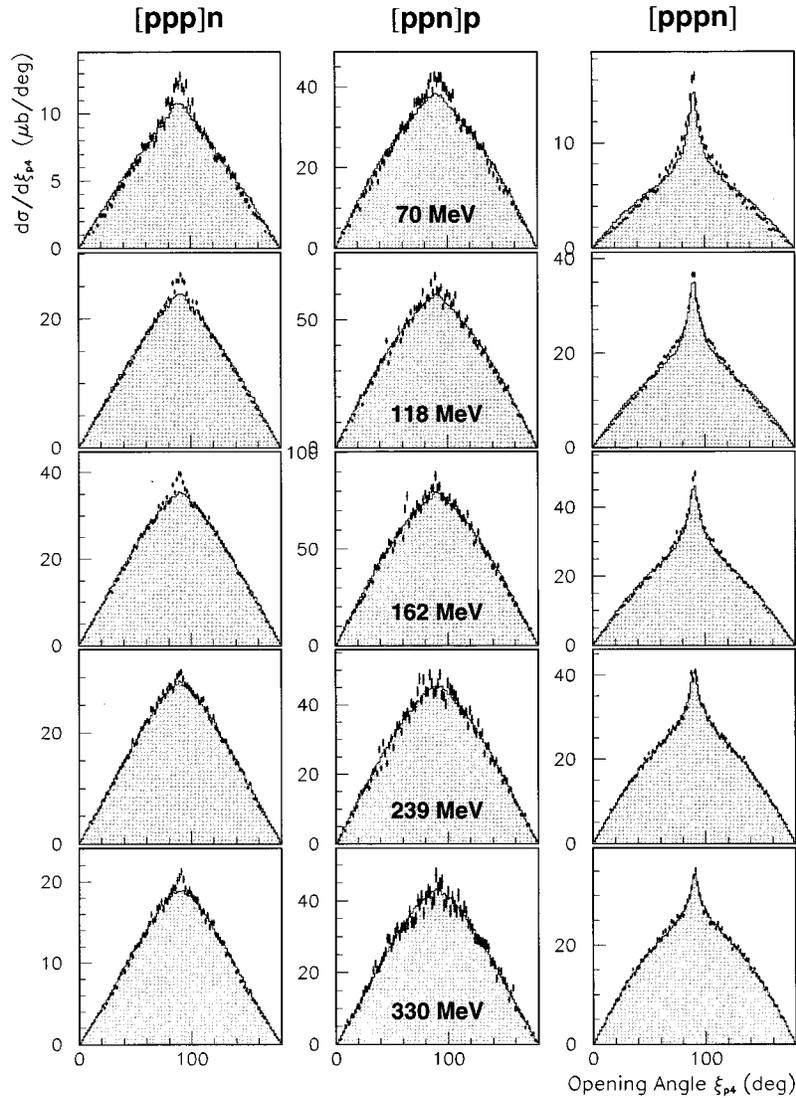
FIG. 13. Distributions over the angle ξ_{p4} between the momentum vector of the fourth particle and the c.m. plane spanned by the other three nucleons for the reaction $\pi^{+4}\text{He} \to pppn$ for incident pion energies of 70, 118, 162, 239, and 330 MeV (from the top) with a threshold of 20 MeV. For further information see Fig. 8.

made with the distributions of modified ISI and HFSI models. The variations of the resulting cross sections with these different distributions usually were well within the cited model uncertainties.

As additional information the $3N$ and $4N$ yields for the reaction $\pi^{+4}\text{He} \to pppn$ with at least three of the emerging nucleons above a threshold of 20 or 30 MeV, respectively, are presented in Table VI. These numbers are less model dependent because almost no extrapolations over unmeasured regions are necessary. The yields are mean values of the results of 10 fits with different variable sets with and without a 2NA tail for each of the two thresholds. These cross sections are pure yields without subtractions of tails of other mechanisms. Here it is interesting to note that even with a threshold of 30 MeV for all four nucleons a significant $4N$ yield remains. This strengthens the fit result that there are processes where all four nucleons are involved in the pion absorption process.

The energy dependence of the cross sections of the reaction $\pi^{+4}\text{He} \to pppn$ is compared in Fig. 15(a) to that of the

reaction $\pi^{+3}\text{He} \to ppp$. In both cases the cross section peaks at an incident pion energy about 30 MeV above the maximum of the quasifree 2NA curve. The shapes of the energy dependence indicate that in both multinucleon reactions an excitation of the Δ resonance may play an important role. However, above the resonance the cross sections of ^4He seem to decrease more slowly than those of ^3He.

In Fig. 15(b) the energy dependences of the partial cross sections of the 3NA channels are compared to those of the 4NA channel. We find that the 3NA(ppn) cross sections are dominant especially at lower energies. Both three-nucleon components show the resonance behavior of the Δ, indicating that $\pi N \to \Delta$ vertices are important in each channel. This conclusion is supported by the observed nonzero angular momentum contributions (see Sec. V B 2). However, the clear resonancelike energy dependence is conspicuously absent from the 4NA data.

The flat shape of the 4NA yield and its small magnitude indicate that the coherent 4NA processes as suggested in Refs. [20–22] cannot play an important role in pion absorp-
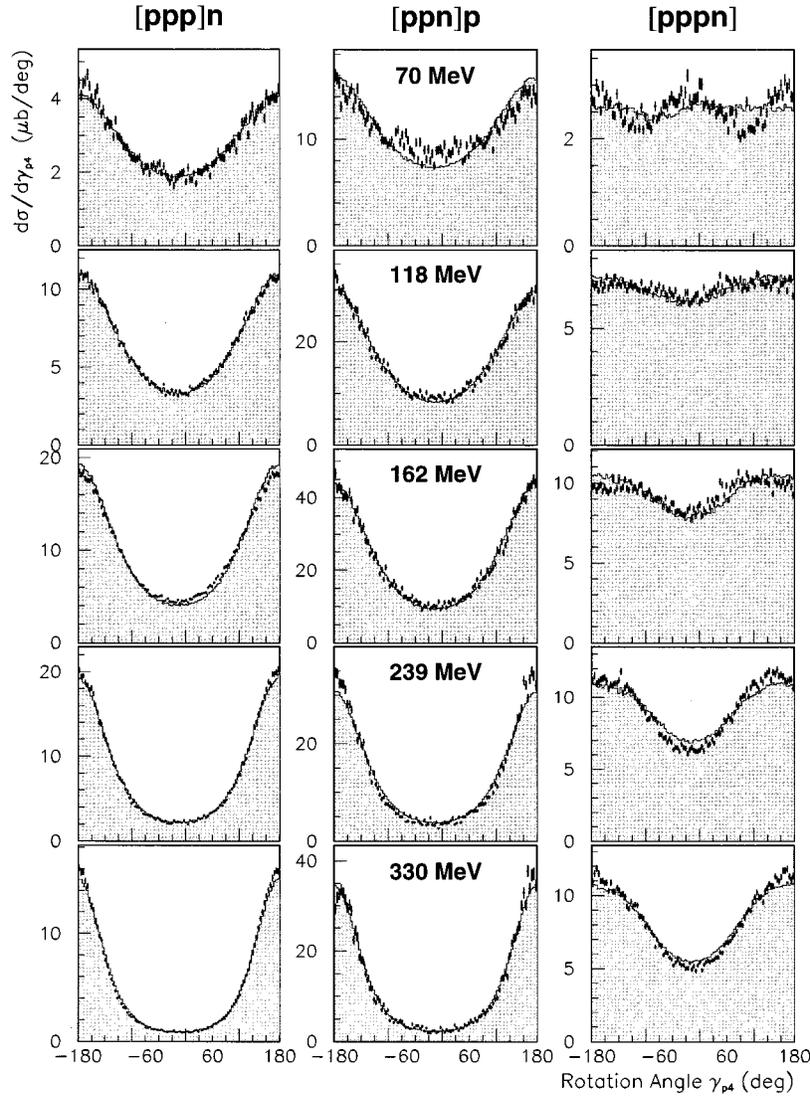
FIG. 14. Distributions over the rotation angle γ_{p4} of the projection of the momentum vector of the slowest particle onto the c.m. plane spanned by the other three nucleons for the reaction $\pi^+{}^4\text{He} \rightarrow pppn$ for incident pion energies of 70, 118, 162, 239, and 330 MeV (from the top) with a threshold of 20 MeV. For further information see Fig. 8.

tion on ^{4}He. The 4NA cross sections measured with this experiment are typically about five times smaller and without the strong energy dependence of the predictions of Ref. [22], in which coherent ''double-Δ'' mechanisms are assumed to be the origin of the multinucleon pion absorption yield.

Compared to the few previous measurements of some multinucleon pion absorption yields on ^{4}He we find that our 3NA(ppp) cross section at 118 MeV of 3.8 ± 0.5 mb is higher than the 2.1 ± 0.4 mb of Ref. [18], while our result at 162 MeV of 5.9 ± 0.7 mb is in agreement with the 4.8 ± 1.0 mb of Ref. [23]. Also our 3NA(ppn) cross section at 118 MeV of 9.8 ± 1.3 mb is significantly larger than the 4.4 ± 1.1 mb of Ref. [18]. The 4NA($pppn$) cross sections at 118 MeV of 0.5 ± 0.13 mb of Ref. [18], and at 120 MeV of 1.0 ± 0.2 mb of Ref. [25] are small compared to our measurement of 1.7 ± 0.2 mb at 118 MeV, while the result at 160 MeV of Ref. [23] of <2 mb agrees with our value of 1.7 ± 0.5 mb. Also the 2.18 ± 0.65 mb at 210 MeV of Ref. [25] is well within the trend of our 4NA cross sections. The discrepan-

cies between our results and the previous data at 120 MeV [18,25] are probably caused by the large extrapolations over phase space that were necessary in these other experiments. Such systematic uncertainties are small in our measurement.

D. Discussion of cross section ratios

The two ^{4}He channels 3NA(ppp) ($T=\frac{3}{2}$) and 3NA (ppn) ($T=\frac{1}{2},\frac{3}{2}$) differ only in their isospin, but this could provide significant insight into the dynamics of the absorption process. Here we may compare the cross section ratio $\sigma_{ppn}/\sigma_{ppp}$ of these two channels with the predictions of our cascade models (ISI,HFSI), based on the isospin ratios of their ingredient steps.

In our very simple models the ISI mechanisms leading to three energetic nucleons are composed of two independent steps. Then the pion scattering cross section of the first and the 2N pion absorption cross section of the second step may be multiplied. Assuming the resonance ratios $\sigma_{\pi^+ p \rightarrow \pi^+ p}/$

TABLE III. Multinucleon cross sections for the reaction $\pi^{+4}\text{He}\rightarrow pppn$ and their fractional decompositions into absorption mechanisms. The numbers are extrapolated to zero threshold. The row $\Sigma\text{ISI}_{(ppn)p}$ stands for the added fractions of the individually fitted models $\text{ISI}_{(ppn)p}$ and $\text{ISI}_{(ppn)p}^{\text{SCX}}$. The errors on the fractional decompositions indicate the stability of the results under the choice of different fitting procedures (see text). The errors on the cross sections also include the normalization uncertainties added in quadrature.

T_π (MeV)	70	118	162	239	330
$\text{ISI}_{(ppp)n}$	1±1 %	1±1 %	4±2 %	8±5 %	9±4 %
$\Sigma\text{ISI}_{(ppn)p}$	9±12 %	3±3 %	4±4 %	16±3 %	13±5 %
(ISI+2NA)	10±13 %	4±4 %	8±4 %	24±6 %	22±7 %
$\text{HFSI}_{(ppp)n}$	6±7 %	4±4 %	1±3 %	0±1 %	1±2 %
$\text{HFSI}_{(ppn)p}$	21±10 %	17±8 %	7±8 %	1±1 %	0±1 %
(2NA+HFSI)	27±16 %	21±10 %	8±9 %	1±1 %	1±2 %
$3\text{NA}_{(ppn)p}^{L\geq0}$	26±7 %	15±7 %	19±6 %	2±2 %	3±3 %
$3\text{NA}_{(ppn)p}^{L\geq1}$	17±9 %	28±5 %	29±7 %	30±3 %	36±6 %
$3N\text{-PS}(ppn)$	43±10 %	43±7 %	48±7 %	32±2 %	39±4 %
$3\text{NA}_{(ppp)n}^{L\geq0}$	3±2 %	10±2 %	12±2 %	3±2 %	0±0 %
$3\text{NA}_{(ppp)n}^{L\geq1}$	11±5 %	11±2 %	15±2 %	23±2 %	19±4 %
$3N\text{-PS}(ppp)$	14±5 %	21±3 %	27±3 %	26±5 %	19±4 %
$4N\text{-PS}(pppn)$	6±3 %	11±2 %	9±3 %	17±1 %	19±4 %
σ_{pppn} (mb)	9.8±1.8	15.3±1.9	18.5±2.1	12.5±1.0	9.3±1.0

$\sigma_{\pi^+n\rightarrow\pi^+n}/\sigma_{\pi^+n\rightarrow\pi^0p}=9/1/2$ and $\sigma_{\pi^+d\rightarrow pp}/\sigma_{\pi^0d\rightarrow pn}\approx2/1$ from charge symmetry, the ratios of the three main ISI processes at the Δ are $\text{ISI}_{(ppp)n}/\text{ISI}_{(ppn)p}/\text{ISI}_{(ppn)p}^{\text{SCX}}\approx9/1/1$, or a 3NA cross section ratio of $\sigma_{ppn}/\sigma_{ppp}\approx2/9$. This ratio is certainly not seen in the cross section ratios of the data (see Table VII), nor in the ratio of ISI yields for the two channels deduced from the fits (see Table III).

A similarly simple picture can be constructed for the HFSI mechanisms. Assuming again that the two basic steps, 2N pion absorption and nucleon rescattering, are independent, the ratio σ_{pn}/σ_{pp} of the NN elastic scattering cross section defines the 3NA ratio to be $\sigma_{ppn}/\sigma_{ppp}\approx2-3$ for HFSI, since the 2NA cross section cancels out. This is close to the ratios seen in the data (see Table VII), which are always larger than one. The ratio of HFSI yields from the fits (Table III) is also in fair agreement with this simple estimate.

These results might suggest that the 3NA yield originates mainly from some final state interactions after the basic 2N pion absorption process. This, however, would be in contradiction to our interpretation of the structures in the data at the higher energies as signatures of ISI, as well as the ratio of ISI to HFSI at these energies deduced from the fits (see Table III).

This apparent contradiction seems to increase the likelihood of a new, unknown process being the origin of most of the 3NA strength. An attempt to explain 3NA by a one-step process was made with a simple model presented in Ref. [19], where only isospin arguments are used to explain the 3NA cross section ratios of $\sigma_{ppp}^{4\text{He}}/\sigma_{ppp}^{3\text{He}}$ and $\sigma_{ppn}/\sigma_{ppp}$. The authors found good agreement with the results from Ref. [18] for the pion energy of 120 MeV.

In Fig. 16 these ratios, measured and calculated, are compared to our data. The horizontal lines indicate the predicted

TABLE IV. Fractions of the multinucleon yields of the possible absorption mechanisms of the reaction $\pi^{+4}\text{He}\rightarrow pppn$ compared to the total pion absorption cross section of ^4He (taken from Ref. [30]).

T_π (MeV)	70	118	162	239
$\sigma_{\text{total}}^{\text{abs}}$ (mb)	35.0±5.3	52.1±3.9	50.5±4.6	26.6±2.0
(ISI+2NA)	3±4 %	1±1 %	3±2 %	11±3 %
(2NA+HFSI)	8±5 %	6±3 %	3±3 %	1±1 %
$3N\text{-PS}(ppn)$	12±4 %	13±3 %	17±4 %	15±2 %
$3N\text{-PS}(ppp)$	4±2 %	6±1 %	10±2 %	12±3 %
$4N\text{-PS}(pppn)$	1±1 %	3±1 %	4±1 %	8±1 %
Total $pppn$	28±7 %	29±4 %	37±5 %	47±5 %

TABLE V. Multinucleon cross sections of the reaction π^{+4}He$\rightarrow pppn$ extrapolated to zero threshold. The full decomposition into the channels 3NA(ppp), 3NA(ppn), and 4NA($pppn$) is also given. The first uncertainties are the standard deviations of the results from the different models and fits, the second reflect the normalization uncertainties.

T_π (MeV)	3NA $\sigma_{(ppp)n}$ (mb)	$\sigma_{(ppn)p}$ (mb)	4NA $\sigma_{(pppn)}$ (mb)	Total σ_{pppn} (mb)
70	$2.0\pm0.6\pm0.3$	$7.2\pm0.6\pm1.2$	$0.6\pm0.3\pm0.1$	$9.8\pm0.8\pm1.6$
118	$3.8\pm0.4\pm0.3$	$9.8\pm1.0\pm0.8$	$1.7\pm0.1\pm0.1$	$15.3\pm1.4\pm1.2$
162	$5.9\pm0.4\pm0.6$	$10.9\pm0.9\pm1.1$	$1.7\pm0.4\pm0.2$	$18.5\pm1.0\pm1.9$
239	$4.3\pm0.2\pm0.3$	$6.0\pm0.5\pm0.5$	$2.2\pm0.2\pm0.2$	$12.5\pm0.4\pm1.0$
330	$2.6\pm0.2\pm0.3$	$4.9\pm1.3\pm0.5$	$1.8\pm0.3\pm0.2$	$9.3\pm0.8\pm0.9$

ratios of Ref. [19] which are both energy independent. In view of the simplicity of the model the agreement with the experimental data is rather good. It should be noted here again, that our 3NA cross sections of ^{4}He are not corrected for losses due to pn pickup reactions in the final state, that lead to deuteronic final states. Taking into account these losses should increase mainly the size of σ_{ppp} at the lower pion energies and could bring the experimentally measured ratio of $\sigma_{ppn}/\sigma_{ppp}$ more in agreement with the predictions. We would like to stress that the model of Ref. [19] currently gives the only simple explanation of the 3NA cross section ratios on ^{3}He and ^{4}He.

VI. SUMMARY AND CONCLUSIONS

In this paper we have presented an analysis of the multinucleon $pppn$ final state after the absorption of a positive pion on ^{4}He for five energies across the Δ resonance. Using a complete set of eight independent variables for this $4N$ final state and simple models, the yield was investigated for contributions from the two-step mechanisms where the basic 2NA process is accompanied by initial or final state interactions. The cross sections of the 3NA(ppp), 3NA(ppn), and 4NA($pppn$) channels were evaluated and compared to each other.

We have shown that p-wave components are important in both the 3NA(ppn) and 3NA(ppp) channel, in order to describe the behavior of the data in noncoplanar geometry. This is consistent with a strong $\pi N\rightarrow\Delta$ coupling of both channels, which is also supported by the energy dependence of the 3NA cross sections. Nevertheless, we find a significant difference between the channels: For 3NA(ppp), a d-wave component seems to become important with increasing incident pion energy, while this is not as evident in the 3NA (ppn) data.

From an investigation of specific differential cross sections we could conclude that there is a significant signal of the ISI mechanism in the 3NA(ppn) channel as well as in the previously investigated 3NA(ppp) channel. Fits to the data suggest a surprisingly strong contribution of ISI to the 3NA(ppn) channel compared to that of the 3NA(ppp) channel, which one would not expect from simple isospin arguments. This suggests that one clue for the solution in explaining the 3NA yield could lie in the initial state.

For the first time an estimate of the contributions from FSI mechanisms (HFSI, SFSI) could be made. The fits to the differential distributions give a HFSI contribution in the $pppn$ final state that exhausts about one quarter of the multinucleon cross section at 70 MeV, but diminishes rapidly at

TABLE VI. $3N$ and $4N$ yields for the reaction π^{+4}He$\rightarrow pppn$ with thresholds of 20 and 30 MeV. The full decomposition into the channels $[ppp]n$, $[ppn]p$, and $[pppn]$ according to the classification scheme of Sec. IV D is given for both thresholds. The first uncertainties are the standard deviations of the results of the different models and fits, the second reflect the normalization uncertainties.

T_N^{thr} (MeV)	T_π (MeV)	$3N$ yield $\sigma_{[ppp]n}$ (mb)	$\sigma_{[ppn]p}$ (mb)	$4N$ yield $\sigma_{[pppn]}$ (mb)	Total σ_{pppn} (mb)
	70	$1.00\pm0.02\pm0.16$	$4.00\pm0.11\pm0.64$	$0.88\pm0.04\pm0.14$	$5.88\pm0.16\pm0.94$
	118	$2.33\pm0.03\pm0.19$	$6.24\pm0.20\pm0.50$	$2.37\pm0.07\pm0.19$	$10.95\pm0.27\pm0.88$
20	162	$3.58\pm0.05\pm0.36$	$8.53\pm0.23\pm0.85$	$3.32\pm0.07\pm0.33$	$15.43\pm0.30\pm1.54$
	239	$2.89\pm0.03\pm0.23$	$4.66\pm0.13\pm0.37$	$3.19\pm0.04\pm0.26$	$10.74\pm0.14\pm0.86$
	330	$1.83\pm0.01\pm0.18$	$4.60\pm0.16\pm0.46$	$2.88\pm0.05\pm0.29$	$9.31\pm0.14\pm0.93$
	70	$0.62\pm0.01\pm0.10$	$2.06\pm0.07\pm0.33$	$0.17\pm0.01\pm0.03$	$2.85\pm0.08\pm0.46$
	118	$1.79\pm0.02\pm0.14$	$4.94\pm0.15\pm0.40$	$0.74\pm0.02\pm0.06$	$7.48\pm0.18\pm0.60$
30	162	$3.17\pm0.03\pm0.32$	$6.64\pm0.17\pm0.66$	$1.40\pm0.02\pm0.14$	$11.21\pm0.21\pm1.12$
	239	$2.93\pm0.04\pm0.24$	$4.98\pm0.06\pm0.40$	$1.73\pm0.01\pm0.14$	$9.65\pm0.07\pm0.77$
	330	$1.99\pm0.01\pm0.20$	$3.90\pm0.15\pm0.39$	$1.91\pm0.02\pm0.19$	$7.80\pm0.16\pm0.78$

TABLE VII. 3NA cross section ratios of the reaction ^{3}He(π^+,ppp) [16] and ^{4}He$(\pi^+,pppn)n$. The isospin ratios $\sigma_{ppn}/\sigma_{ppp}$ (three rightmost columns) are given for 0, 20, and 30 MeV thresholds. The uncertainties include both fit and normalization errors.

T_π (MeV)	$\sigma_{ppp}^{^4\text{He}}/\sigma_{ppp}^{^3\text{He}}$ $T_N^{\text{thr}}=0$ MeV	$T_N^{\text{thr}}=0$ MeV	$\sigma_{ppn}/\sigma_{ppp}$ $T_N^{\text{thr}}=20$ MeV	$T_N^{\text{thr}}=30$ MeV
70	0.7 ± 0.3	3.6 ± 1.3	4.0 ± 0.9	3.3 ± 0.8
118	0.6 ± 0.1	2.6 ± 0.5	2.7 ± 0.3	2.8 ± 0.3
162	0.8 ± 0.1	1.8 ± 0.3	2.4 ± 0.3	2.1 ± 0.3
239	1.1 ± 0.1	1.4 ± 0.2	1.6 ± 0.2	1.7 ± 0.2
330	2.3 ± 0.5	1.8 ± 0.6	2.5 ± 0.4	2.0 ± 0.3

higher energies. The HFSI yield in the 3NA(ppn) channel is found to be stronger than that in the 3NA(ppp) channel. Both this energy dependence and the ratio HFSI(ppn)/HFSI (ppp) follow about the behavior of the NN elastic cross sections. We were also able to roughly evaluate the SFSI yield in the 3NA(ppn) and 4NA($pppn$) channels to be a few percent of these multinucleon absorption cross sections, becoming less important at higher pion energies.

Despite the evidence of ISI and FSI mechanisms being the origin of a part of the multinucleon absorption cross section on ^{4}He, a large fraction (about two thirds) of the yield cannot be accounted for by our simple models. However, if one allows nonzero angular momentum components, the dis-

tributions of the remaining strength are reasonably well reproduced by simple $3N$ and $4N$ phase space models. On the other hand, we know that HFSI and $3N$-PS models are not easily distinguishable by signatures [16]. Since the 3NA ratios $\sigma_{ppn}/\sigma_{ppp}$ are broadly understandable in terms of the elastic NN cross sections an explanation of most of the 3NA yield in terms of HFSI, in spite of the results of our fits, might seem plausible. However, this would imply that final state distortions are more important than initial state ones, despite the much larger (at and above resonance) πN cross section.

The key to solve these ambiguities may be given by the simple isospin considerations discussed in Ref. [19]. Assuming a one-step 3NA process and an equal size for the two isospin amplitudes $F_{1/2}$ and $F_{3/2}$ the 3NA cross section ratios $\sigma_{ppp}^{^4\text{He}}/\sigma_{ppp}^{^3\text{He}}$ and $\sigma_{ppn}/\sigma_{ppp}$ of ^{4}He were related to each other. In view of the simplicity of the model the agreement with our data is good. This result would also match the observation from the fits of a large fraction of noncascade 3NA yield. However, the model of Ref. [19] says nothing specific about the underlying 3NA mechanism. In this respect the unexplained structures visible in the differential cross sections could become important.

We have also measured the 4NA cross sections for the first time in an experiment detecting a large part of the yield
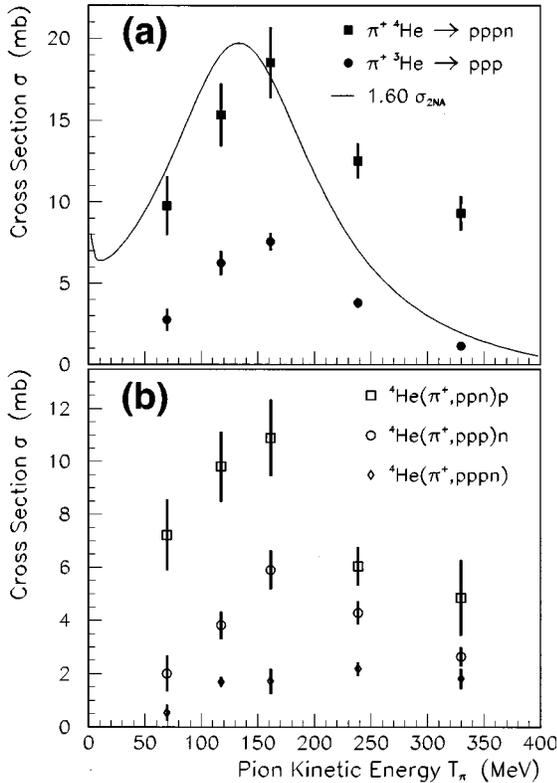

FIG. 15. (a) Multinucleon cross sections σ_{ppp} and σ_{pppn} for the reactions π^{+3}He$\rightarrow ppp$ and π^{+4}He$\rightarrow pppn$, respectively. The curve represents the 2NA cross section (arbitrarily normalized) as parametrized in Ref. [37]. (b) Decomposition of the ^{4}He $pppn$ absorption yield into the 3NA absorption channels 3NA(ppp) and 3NA(ppn), and the 4NA absorption channel 4NA($pppn$).
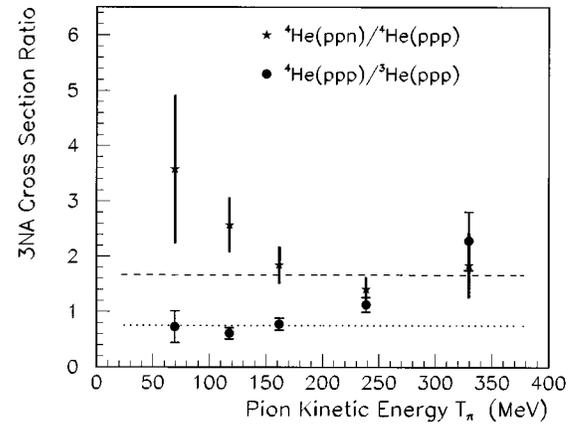

FIG. 16. Ratios between the 3NA cross sections $\sigma_{ppp}^{^4\text{He}}$ and $\sigma_{ppp}^{^3\text{He}}$ and between the two isospin different 3NA channels 3NA(ppn) and 3NA(ppp) of ^{4}He. The experimental data are compared to the isospin ratios deduced in Ref. [19]: $\sigma_{ppp}^{^4\text{He}}/\sigma_{ppp}^{^3\text{He}}$ (dotted line) and $\sigma_{ppn}/\sigma_{ppp}$ of ^{4}He (dashed line).

from this relatively weak process directly. Neither the distributions nor the energy dependence of these cross sections suggest that the ''double-Δ'' [21,22] is an important mechanism at these energies. Although these 4NA distributions have not been examined in as great detail as those of 3NA, there are indications in the data that sequential processes (ISI) play a role in parallel to the statistical features of the 4NA events.

In conclusion, we have established the strength and behavior of 3NA, in both the 3NA(ppp) and 3NA(ppn) channels, and of 4NA on ^{4}He. The 3NA is broadly interpretable in terms of a mixture of ISI, FSI, and a large phase-space-like component. However, some structures in the distributions and the relative strengths of ISI and FSI are still unexplained. Thus it remains an open question whether a coherent description of 3NA, including interference effects, could better explain these features.

[1] D. Ashery and J. P. Schiffer, Annu. Rev. Nucl. Part. Sci. **36**, 207 (1986).

[2] H. J. Weyer, Phys. Rep. **195**, 295 (1990).

[3] C. H. Q. Ingram, Nucl. Phys. **A553**, 573c (1993).

[4] K. Ohta, M. Thies, and T.-S. H. Lee, Ann. Phys. (N.Y.) **163**, 420 (1985).

[5] G. Backenstoss, M. Izycki, P. Salvisberg, M. Steinacher, P. Weber, H. J. Weyer, S. Cierjacks, S. Ljungfelt, H. Ullrich, M. Furić, and T. Petković, Phys. Rev. Lett. **55**, 2782 (1985).

[6] K. A. Aniol, A. Altman, R. R. Johnson, H. W. Roser, R. Tacik, U. Wienands, D. Ashery, J. Alster, M. A. Moinester, E. Piasetzky, D. R. Gill, and J. Vincent, Phys. Rev. C **33**, 1714 (1986).

[7] L. C. Smith, R. C. Minehart, D. Ashery, E. Piasetsky, M. Moinester, I. Navon, D. F. Geesaman, J. P. Schiffer, G. Stephens, B. Zeidman, S. Levinson, S. Mukhopadhyay, R. E. Segel, B. Anderson, R. Madey, J. Watson, and R. R. Whitney, Phys. Rev. C **40**, 1347 (1989).

[8] P. Weber, G. Backenstoss, M. Izycki, R. J. Powers, P. Salvisberg, M. Steinacher, H. J. Weyer, S. Cierjacks, A. Hoffart, B. Rzehorz, H. Ullrich, D. Bosnar, M. Furić, T. Petković, and N. Šimičević, Nucl. Phys. **A534**, 541 (1991).

[9] S. Mukhopadhyay, S. Levenson, R. E. Segel, G. Garino, D. Geesaman, J. P. Schiffer, G. Stephans, B. Zeidman, E. Ungricht, H. Jackson, R. Kowalczyk, D. Ashery, E. Piasetsky, M. Moinester, I. Navon, L. C. Smith, R. C. Minehart, G. S. Das, R. R. Whitney, R. Mckeown, B. Anderson, R. Madey, and J. Watson, Phys. Rev. C **43**, 957 (1991).

[10] P. Salvisberg, G. Backenstoss, H. Krause, R. J. Powers, M. Steinacher, H. J. Weyer, M. Wildi, A. Hoffart, B. Rzehorz, H. Ullrich, D. Bosnar, M. Furić, T. Petković, N. Šimičević, H. Zmeskal, A. Janett, and R. H. Sherman, Phys. Rev. C **46**, 2172 (1992).

[11] T. Alteholz, D. Androić, G. Backenstoss, D. Bosnar, H. Breuer, A. Brković, H. Döbbeling, T. Dooling, W. Fong, M. Furić, P. A. M. Gram, N. K. Gregory, J. P. Haas, A. Hoffart, C. H. Q. Ingram, A. Klein, K. Koch, J. Köhler, B. Kotliński, M. Kroedel, G. Kyle, A. Lehmann, Z. N. Lin, G. Mahl, A. O. Mateos, K. Michaelian, S. Mukhopadhyay, T. Petković, R. P. Redwine, D. Rowntree, R. Schumacher, U. Sennhauser, N. Šimičević, F. D. Smit, G. van der Steenhoven, D. R. Tieger, R. Trezeciak, H. Ullrich, M. Wang, M. H. Wang, H. J. Weyer, M. Wildi, and K. E. Wilson, Phys. Rev. Lett. **73**, 1336 (1994).

[12] H. Hahn, A. Altman, D. Ashery, G. Gefen, D. R. Gill, R. R. Johnson, R. Levy-Nathansohn, M. A. Moinester, M. Sevior, and R. P. Trelle, Phys. Rev. C **53**, 1074 (1996).

[13] G. Backenstoss, M. Izycki, R. Powers, P. Salvisberg, M. Steinacher, P. Weber, H. J. Weyer, A. Hoffart, B. Rzehorz, H. Ullrich, D. Bosnar, M. Furić, and T. Petković, Phys. Lett. B **222**, 7 (1989).

[14] G. Backenstoss, D. Bosnar, H. Breuer, H. Döbbeling, T. Dooling, M. Furić, P. A. M. Gram, N. K. Gregory, A. Hoffart, C. H. Q. Ingram, A. Klein, K. Koch, J. Köhler, B. Kotliński, M. Kroedel, G. Kyle, A. Lehmann, A. O. Mateos, K. Michaelian, T. Petković, R. P. Redwine, D. Rowntree, U. Sennhauser, N. Šimičević, R. Trezeciak, H. Ullrich, M. Wang, M. H. Wang, H. J. Weyer, M. Wildi, and K. E. Wilson, Phys. Lett. B **379**, 60 (1996).

[15] D. Androić, G. Backenstoss, D. Bosnar, H. Breuer, H. Döbbeling, T. Dooling, M. Furić, P. A. M. Gram, N. K. Gregory, A. Hoffart, C. H. Q. Ingram, A. Klein, K. Koch, J. Köhler, B. Kotliński, M. Kroedel, G. Kyle, A. Lehmann, A. O. Mateos, K. Michaelian, T. Petković, R. P. Redwine, D. Rowntree, U. Sennhauser, N. Šimičević, R. Trezeciak, H. Ullrich, M. Wang, M. H. Wang, H. J. Weyer, M. Wildi, and K. E. Wilson, Phys. Rev. C **53**, R2591 (1996).

[16] A. Lehmann, D. Androić, G. Backenstoss, D. Bosnar, H. Breuer, H. Döbbeling, T. Dooling, M. Furić, P. A. M. Gram, N. K. Gregory, A. Hoffart, C. H. Q. Ingram, A. Klein, K. Koch, J. Köhler, B. Kotliński, M. Kroedel, G. Kyle, A. O. Mateos, K. Michaelian, T. Petković, M. Planinić, R. P. Redwine, D. Rowntree, U. Sennhauser, N. Šimičević, R. Trezeciak, H. Ullrich, M. Wang, M. H. Wang, H. J. Weyer, M. Wildi, and K. E. Wilson, Phys. Rev. C **55**, 2931 (1997).

[17] H. Kamada, M. P. Locher, T.-S. H. Lee, J. Golak, V. E. Markushin, W. Glöckle, and H. Witala, Phys. Rev. C **55**, 2563 (1997).

[18] M. Steinacher, G. Backenstoss, M. Izycki, P. Salvisberg, P. Weber, H. J. Weyer, A. Hoffart, B. Rzehorz, H. Ullrich, M. Dzemidzić, M. Furić, and T. Petković, Nucl. Phys. **A517**, 413 (1990).

[19] A. Mateos and N. Šimičević, Phys. Rev. C **47**, R1842 (1993).

[20] V. M. Kolybasov, Sov. J. Nucl. Phys. **3**, 535 (1966); V. M. Kolybasov *ibid.* **3**, 704, (1966); V. M. Kolybasov and T. A.

Lomonosova, *ibid.* **11**, 325 (1970); V. M. Kolybasov and V. A. Tsepov, *ibid.* **14**, 418 (1972).

[21] G. E. Brown, H. Toki, W. Weise, and A. Wirzba, Phys. Lett. **118B**, 39 (1982).

[22] B. Schwesinger, A. Wirzba, and G. E. Brown, Phys. Lett. **132B**, 269 (1983).

[23] P. Weber, J. McAlister, R. Olszewski, A. Feltham, M. Hanna, R. Johnson, M. Pavan, C. Ponting, F. Rozon, M. Sevior, V. Sossi, D. Vetterli, D. Humphrey, G. Lolos, Z. Papandreou, R. Tacik, D. Ottewell, G. Sheffer, G. Smith, Y. Mardor, and S. May-Tal, Phys. Rev. C **43**, 1553 (1991).

[24] L. C. Smith, R. C. Minehart, O. K. Baker, D. B. Day, K. L. Giovanetti, R. Lourie, R. M. Marshall, B. Milbrath, B. G. Ritchie, R. M. Sealock, D. Tedeschi, and S. T. Thornton, Phys. Rev. C **48**, R485 (1993).

[25] B. Rzehorz, G. Backenstoss, M. Džemidžic, M. Furić, A. Hoffart, T. Petković, H. Ullrich, H. J. Weyer, D. Weiser, and M. Wildi, Europhys. Lett. **34**, 103 (1996).

[26] T. Alteholz, D. Androić, G. Backenstoss, D. Bosnar, H. Breuer, A. Brković, H. Döbbeling, T. Dooling, W. Fong, M. Furić, P. A. M. Gram, N. K. Gregory, J. P. Haas, A. Hoffart, C. H. Q. Ingram, A. Klein, K. Koch, J. Köhler, B. Kotliński, M. Kroedel, G. Kyle, A. Lehmann, Z. N. Lin, G. Mahl, A. O. Mateos, K. Michaelian, S. Mukhopadhyay, T. Petković, M. Planinić, R. P. Redwine, D. Rowntree, R. Schumacher, U. Sennhauser, N. Šimičević, F. D. Smit, G. van der Steenhoven, D. R. Tieger, R. Trezeciak, H. Ullrich, M. Wang, M. H. Wang, H. J. Weyer, M. Wildi, and K. E. Wilson, Nucl. Instrum. Methods Phys. Res. A **373**, 374 (1996).

[27] A. Mateos, Ph.D. thesis, MIT, 1995.

[28] R. Trezeciak, Ph.D. thesis, University of Karlsruhe, 1995.

[29] J. Köhler, Ph.D. thesis, University of Basel, unpublished.

[30] A. O. Mateos, D. Androić, G. Backenstoss, D. Bosnar, H. Breuer, H. Döbbeling, T. Dooling, M. Furić, P. A. M. Gram, N. K. Gregory, A. Hoffart, C. H. Q. Ingram, A. Klein, K. Koch, J. Köhler, B. Kotliński, M. Kroedel, G. Kyle, A. Lehmann, K. Michaelian, T. Petković, M. Planinić, R. P. Redwine, D. Rowntree, U. Sennhauser, N. Šimičević, R. Trezeciak, H. Ullrich, M. Wang, M. H. Wang, H. J. Weyer, M. Wildi, and K. E. Wilson, submitted to Phys. Rev. C.

[31] R. Schiavilla, V. R. Pandharipande, and R. B. Wiringa, Nucl. Phys. **A449**, 219 (1986).

[32] R. Schiavilla, private communication.

[33] J. F. J. van den Brand, H. P. Blok, R. Ent, E. Jans, J. M. Laget, L. Lapikás, C. de Vries, and P. K. A. de Witt Huberts, Nucl. Phys. **A534**, 637 (1991).

[34] N. Šimičević and A. Mateos, Phys. Rev. C **51**, 797 (1995).

[35] SCATPI, J. B. Walter and G. A. Rebka, Los Alamos National Laboratory Report LA-7731-MS, 1979.

[36] R. A. Arndt, L. D. Roper, R. A. Bryan, R. B. Clark, B. J. VerWest, and P. Signell, Phys. Rev. D **28**, 97 (1983); R. A. Arndt, L. D. Roper, R. L. Workman, and M. W. McNaughton, *ibid.* **45**, 3995 (1992); SAID, R. A. Arndt *et al.*, Virginia Polytechnic Institute, 1988.

[37] B. G. Ritchie, Phys. Rev. C **44**, 533 (1991).

[38] J. Gillespie, *Final-State Interactions* (Holden-Day, San Francisco, 1965).

[39] B. Zeitnitz, R. Maschuw, and P. Suhr, Nucl. Phys. **A149**, 449 (1970).

[40] R. Taylor, *Scattering Theory* (Wiley, New York, 1972), pp. 424–432.

[41] K. Watson, Phys. Rev. **88**, 1163 (1952); A. B. Migdal, Sov. Phys. JETP **1**, 2 (1955); M. L. Goldberger and K. M. Watson, *Collision Theory* (Wiley, New York, 1964).

[42] E. M. Henley, unpublished.

[43] K. Wilson, Ph.D. thesis, MIT, 1995.